



Utrecht  
University



# THE ROLE OF THE EXCAVATING SPONGE *CLIONA CELATA* IN OYSTER SHELLS

MASTER THESIS BY ENZO MARTINO KINGMA  
7076274

NIOZ  
Utrecht University  
04-02-2022

## The role of the excavating sponge *Cliona celata* in oyster shells

### Master Thesis in partial fulfilment of the degree of Master of Science in Marine Sciences at the Utrecht University, The Netherlands

**Study program:** MSc Marine Sciences

**Name student:** Enzo Martino Kingma

**Registration number:** 7076274

#### **Supervisors:**

1st supervisor Paolo Stocchi

2nd supervisor Lennart de Nooijer

3rd supervisor Gert-Jan Reichart

#### **Examiner:**

Gert-Jan Reichart

# Contents

<b>Abstract.....</b>	<b>5</b>
<b>Introduction.....</b>	<b>1</b>
1.1 Oyster reefs at risk.....	1
1.2 The carbonate budget of oyster reefs.....	1
1.3 Excavating sponges.....	2
1.4 <i>Cliona celata</i> .....	3
1.5 Bioerosion by clinoid sponges.....	3
1.6 Relevance.....	5
1.7 Research questions.....	5
<b>Methods.....</b>	<b>6</b>
2.1 Collection, sampling and instalment.....	6
2.2 Microscopy analysis.....	6
2.2.1 Scanning electron microscopy and processing of the images.....	6
2.2.2 Fluorescence microscopy.....	6
<i>Calibration</i> .....	7
<i>Incubation and sample preparation</i> .....	7
<i>Photographs and processing</i> .....	8
<i>Python</i> .....	8
<i>Software</i> .....	9
<i>Local flux</i> .....	9
<b>Results.....</b>	<b>10</b>
3.1 Scanning electron microscope images.....	10
3.2 Fluorescence microscope images.....	14
3.3 Local flux.....	15
<b>Discussion.....</b>	<b>16</b>
4.1 Scanning electron microscope images.....	16
4.2 Fluorescence microscope.....	17
4.3 Recommendations and limmitations.....	19
4.3.1 Materials.....	19
4.3.2 Sample preparation.....	19
4.3.3 Calibration.....	20
4.3.4 Microscopy analysis.....	20
4.3.5 Flux calculation.....	20
4.4 Future state of excavating sponges.....	21
<b>Conclusion.....</b>	<b>21</b>
<b>Acknowledgements.....</b>	<b>22</b>
<b>References.....</b>	<b>23</b>
<b>Appendix.....</b>	<b>27</b>
Appendix A.....	27
Appendix B.....	29
Appendix C.....	30

## List of Figures

<b>Figure 1.</b> Main ecosystem services provided by oyster reefs.....	1
<b>Figure 2.</b> Carbon budget of oyster reefs.....	2
<b>Figure 3.</b> Traces of <i>C. celata</i> in oyster shell .....	2
<b>Figure 4.</b> Map occurrence <i>Cliona celata</i> in The Netherlands.....	3
<b>Figure 5.</b> SEM image depicting excavation by <i>C. celata</i> on calcite.....	4
<b>Figure 6.</b> Conceptual model for chemical dissolution of $\text{CaCO}_3$ by excavating sponges.....	4
<b>Figure 7.</b> Radiometric application of HPTS as a function of pH.....	7
<b>Figure 8.</b> Output scan fluorescence microscope.....	8
<b>Figure 9.</b> Raw data fluorescence microscope.....	8
<b>Figure 10.</b> SEM images initial stage bioerosion.....	10
<b>Figure 11.</b> SEM images showing etching marks, pits and chips.....	11
<b>Figure 12.</b> SEM images pitted holes.....	12
<b>Figure 13.</b> SEM images tunnel formation.....	13
<b>Figure 14.</b> Timeline erosion development by <i>C. celata</i> on Iceland spar.....	13
<b>Figure 15.</b> HPTS pH maps.....	14
<b>Figure 16.</b> Transect proton concentration.....	15
<b>Figure 17.</b> Schematic representation of calcite chip.....	18
<b>Figure 18.</b> Sponge-spar attachment.....	19
<b>Figure 19.</b> Example pH map output created in python .....	28
<b>Figure 20.</b> Determination pit depth.....	29
<b>Figure 21.</b> Determination of eroded surface area.....	29
<b>Figure 22.</b> Proton concentration transects.....	30

## Abstract

Excavating sponges are the most common and destructive macro-eroders present in carbonate dominated habitats, such as coral- and oyster reefs. These sponges penetrate in carbonate skeletons and shells, forming a complex network of tunnels and chambers. In temperate climates, their presence can pose a threat to services provided by oyster reefs due to weakening and damaging the oyster shells, which in the long term leads to loss of the reef structure. Sponge bioerosion proceeds by a combination of chemical dissolution and mechanical chip removal. However, the exact chemical conditions during sponge bioerosion are largely unknown. Here, we provided insights into the bioeroding mechanism of *Cliona celata* present in oyster shells collected from the Grevelingenmeer and the Oosterschelde, The Netherlands. By growing *C. celata* on pieces of Iceland spar (a pure transparent form of crystalline calcium carbonate) the conditions of dissolution at the sponge-CaCO<sub>3</sub> interface were investigated. Using a pH fluorescent probe followed by fluorescence microscopy, we were able to show that the intracellular pH at this interface is lower compared to ambient seawater. This suggests active proton pumping and release of low pH bundles, to be responsible for creating an acidic microenvironment and hence promoting dissolution of CaCO<sub>3</sub>. Using a model based on the linear Heat-Diffusion equation, we estimated a local proton flux of  $3.02 \times 10^{-8} \text{ mol dm}^{-2} \text{ s}^{-1}$  towards the edge of the sponge tissue where etching takes place. Additionally, using scanning electron microscopy we showed that bioerosion by *C. celata* occurs in successive phases; from dissolution of lattice deficiencies, to etching marks that over time form well-developed pitted holes/tunnels and chips.

This study adds to the understanding of the mechanisms that drive sponge bioerosion and provides more insight on how environmental conditions can affect calcium carbonate dissolution by excavating sponges as well as making predictions about future rates of sponge activity.

### Keywords

*Bioerosion - Excavating sponges - Cliona celata - Fluorescence microscopy - Grevelingenmeer*

# Introduction

## 1.1 Oyster reefs at risk

Oysters are considered valuable ecosystem engineers, because they contribute to numerous ecosystem functions and services (Figure 1; Jones et al., 1994; Lemasson et al., 2017). Oyster reefs provide habitat and food for many species, but they can also play a major role in stabilizing the coastline and suppressing erosion. Oysters are filter feeders and thereby play a role in shallow water benthic-pelagic coupling. Additionally, oysters are harvested for human consumption and provide cultural services related to recreational and educational uses. Other important services include nutrient cycling and carbon sequestration (Paolisso & Dery, 2010, Scyphers et al., 2014). However, currently many oyster reef ecosystems are in a poor state due to climate change, pollution and mechanical disturbance. For example, ocean acidification negatively affects all stages of the oyster life cycle and intensive fisheries can deteriorate the state of oyster beds (Lemasson et al., 2017; Bennema et al., 2020). A study by Beck et al. (2011) estimated that 85% of all native oyster reefs worldwide have disappeared and current reefs represent less than 10% of what was historically present, therefore the reefs can be considered functionally extinct. On top of climate change and pollution, excavating sponges pose an additional threat to the integrity of these ecosystems. These sponges may deteriorate the dynamic balance between reef growth and bioerosion, which can reverse the direction of the inorganic carbon flux.

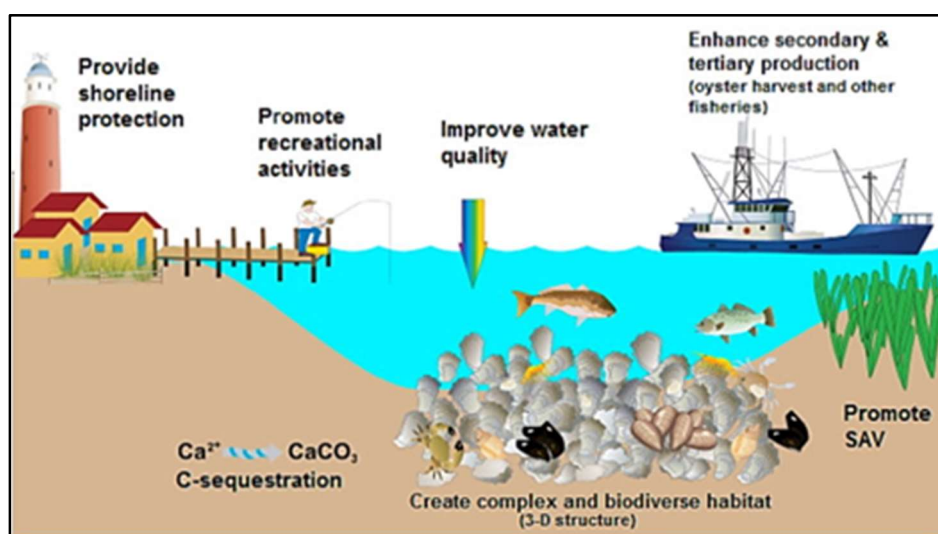


Figure 1: The main ecosystem services provided by oyster reefs (SAV= Submerged Aquatic Vegetation). Figure adapted from Lemasson et al. (2017).

## 1.2 The carbonate budget of oyster reefs

The net carbon deposition in oyster reefs can be calculated by subtracting carbon losses from carbon deposition. Carbon deposition includes calcification, biomass accumulation and sediment accretion, and losses include respiration, calcification and bioerosion (Figure 2; Lee et al., 2020). Oysters are important calcifying organisms, they can sequester vast amounts of carbon by accumulating calcium carbonate crystals as subsequent shell layers. The carbonate budget in oyster reefs, similar as with other calcareous reefs such as coral reefs, is primarily determined by the balance between growth (calcification) and breakdown (erosion) (Perry et al., 2014; Webb et al., 2017). Erosion takes place by severe storms like hurricanes that have shown to set back growth and development of oyster reefs (Livingston et al., 1999).

The effect of such storms, however, is limited in The Netherlands. In contrast to the physical erosion of oyster reefs, bioerosion is a much more common and continuous process (Kennedy et al., 2013). Neumann (1966) defined bioerosion as the destruction and removal of consolidated mineral or lithic substrate by the direct action of organisms. According to Dunn et al. (2014) the decline of subtidal oyster reefs often coincides with an increased prevalence of excavating sponges present in the oysters' shells. Bioerosion can reach levels that damage the whole structural integrity of calcareous reefs (Rützler, 1975). In healthy systems there is a balance between the constructive and destructive forces of calcareous reefs. Taking a closer look at this balance in oyster reefs allows us to determine the impact of excavating sponges and predict future reef growth performance and trajectories.

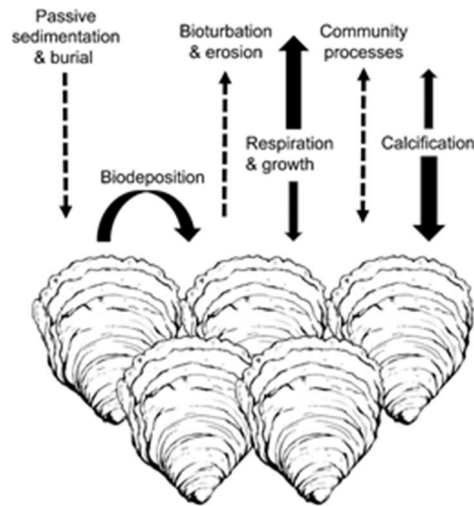


Figure 2: Carbon budget of oyster reefs. The direction of the arrows indicates carbon deposition (downward) or carbon release (upward). The arrow size gives an indication of the relative size of carbon flow, but is dependent on environmental conditions. Figure adapted from Lee et al. (2020).

### 1.3 Excavating sponges

Excavating sponges are capable of boring in carbonate material forming a complex 3D-network of chambers and tunnels. They thereby have a significant effect on the functioning of for example coral reefs and potentially, on whole reef biogeochemistry (Webb et al., 2019a). Despite the fact that they live inside calcareous material, bioeroding sponges are filter feeders and in some cases form a symbiotic relationship with Symbiodinium dinoflagellates (Schönberg & Loh 2005; Weisz et al., 2010; Schönberg & Wisshak, 2012).

In many marine systems, excavating sponges are among the most dominant and important macro-eroders of calcareous substrates, such as in coral reefs and mollusc beds (Wisshak et al., 2014; De Bakker et al., 2018). This study primarily focuses on the role of the excavating sponge *Cliona celata* (Grant, 1826), which in The Netherlands is mainly found inhabited in old (i.e. empty) oyster shells. *C. celata* penetrates the oyster shells to seek shelter which can lead to severe shell damage and is therefore also often called oyster pest (Figure 3).

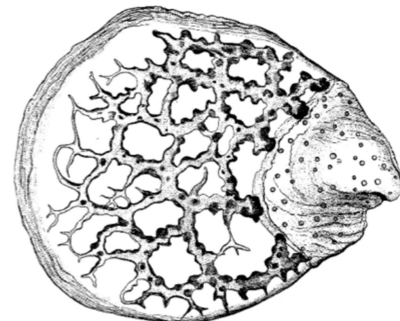


Figure 3: Traces of *C. celata* in oyster shell according to Hancock et al. (1849).

## 1.4 *Cliona celata*

*C. celata* tolerates a large variety of environmental stressors such as high nutrient loads, low salinity, and large temperature fluctuations (Hartman, 1957; Carballo et al., 1996). It is therefore no surprise that *C. celata* can be found in a wide range of ecological environments with varying physical conditions, from mean low water up to 200 meters depth in wave exposed, open coasts and silty estuaries (Hartman, 1958; Snowden, 2007). The optimal temperature range for *C. celata* lies between 10-20 °C and growth is temperature dependent (Cobb, 1969). Greatest abundance is recorded in waters with a little lowered salinity level (25-30 ppt) (Hartman, 1958; Nicol & Reisman, 1976). The sponge is able to tolerate high levels of sedimentation and turbidity (<4m visibility), which means that this species can be encountered in more muddy environments (Carballo et al., 1994; Carballo & Bell, 2017). However excessive sedimentation may hamper colonization (Nicol & Reisman, 1976).

In The Netherlands *C. celata* is widespread observed burrowed in old bivalve shells, mostly in both living and dead oyster shells present in the Oosterschelde and the Grevelingenmeer, but also in the Wadden Sea and North Sea, Figure 4 (Hoeksema, 1983; Bennema., 2014). During the fieldwork for this study no *C. celata* was encountered in the oyster reefs at Texel (surrounding the ferry at 't Horntje and near De Cocksdorp). *C. celata* was however, abundantly found in the oyster reefs in the Grevelingenmeer and the Oosterschelde at locations with lower turbidity (between 5-15 meters deep), mostly infested in *Crassostrea gigas* and a few in *Ostrea edulis*.

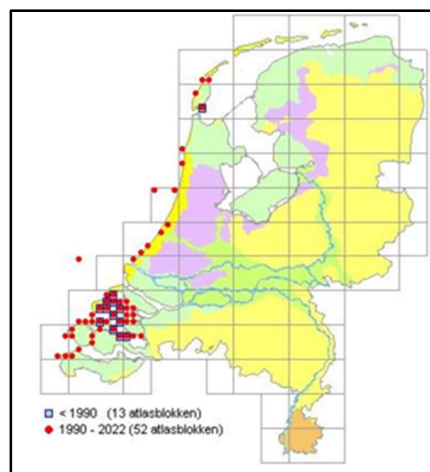


Figure 4: Occurrence of *Cliona celata* in The Netherlands.  
Figure adapted from Bennema (2022).

The presence of *C. celata* in the oyster shell can cause several effects on the oysters. Damage caused by *C. celata* can lead to the entry of sand and mud in living oysters. Tunnels created by *Cliona* can become inhabited by other organisms, like polychaete worms (Bower et al., 1994). The presence of *Cliona* has an influence on all oyster life stages. It reduces larval settlement and increases larval mortality (Barnes et al., 2010). It has even shown to lower the overall production of larvae in oyster reefs (Bahr & Hillman, 1967; Davis & Hillman 1971). Erosion by these sponges may also lead to a higher predation risk from crushing and drilling predators as shells lose their structural integrity and a damaged hinge mechanism (the protective device against their predators) makes the oysters more vulnerable (Thomas, 1979; Stefaniak et al., 2005; Buschbaum et al., 2007). Eventually when boring by the sponge starts to exceed shell repair, the shell weakens which results in an increased mortality of the oysters (Guida, 1977; Bower et al., 1994).

## 1.5 Bioerosion by clinoid sponges

While the general process of sponge bioerosion is known, the exact chemical and physical conditions are only partially understood. Bioerosion by clinoid sponges occurs as a combination of mechanical chip removal and chemical dissolution. These sponges contain specialized etching cells called amoebocytes which are capable of removing calcite chips by etching and chipping away carbonate fragments (Pomponi, 1979; Rützler & Rieger, 1973). Etching cells gradually penetrate the calcareous substrate by localized dissolution of calcium carbonate due to the release of an acidic etching agent until a chip gets etched free and a pit is formed (Cobb, 1969). This process is repeated over and over and

leads to the formation of a 3D-network (Figure 5). However, many uncertainties remain about the exact bioerosion mechanism. For example, little progress has been made to identify the etching agent (Hatch, 1980; Webb et al., 2019b).

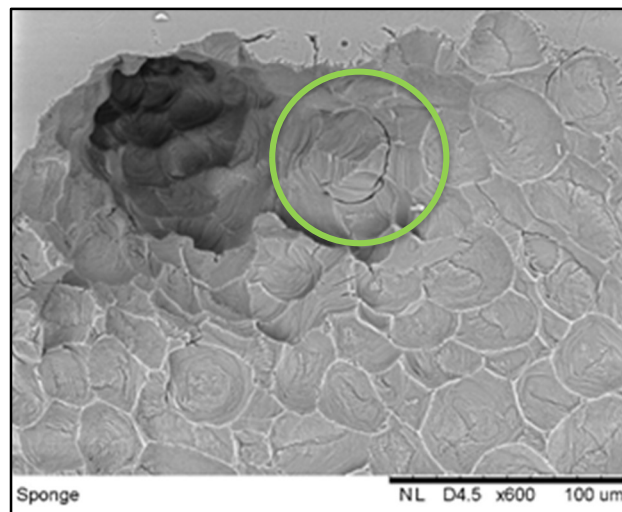


Figure 5: Scanning electron microscope image depicting excavation by *C. celata* on calcite (Iceland spar). In the green circle is the formation of a new chip that has not yet been removed.

It is hypothesized that these sponges are capable of adjusting the carbonate solubility equilibrium, in the favour of carbonate dissolution, by the release of protons ( $H^+$ ) from the etching cells (Hatch, 1980). Hatch (1980) demonstrated that the presence of the enzyme carbonic anhydrase, at the etching interface between the sponge and carbonate material, promotes proton transport across the sponge membrane which would then lower the carbonate saturation state in a so-called microenvironment (Figure 6). This also provides optimal pH inside the sponge tissue for other processes as calcium chelators. Calcium chelators enable a type of dissolution cycle where protons are received in exchange for calcium ions from the surrounding seawater and are then released from the sponge tissue at the etching interface in return for calcium ion uptake (Sullivan et al., 1986; Rützler, 1971). However, as Webb et al. (2019) mentioned whether this process is adopted by excavating sponges has still to be confirmed. But in theory this does provide a process cycle which suggests that local lowering of the pH is responsible for chemical dissolution of  $CaCO_3$ .

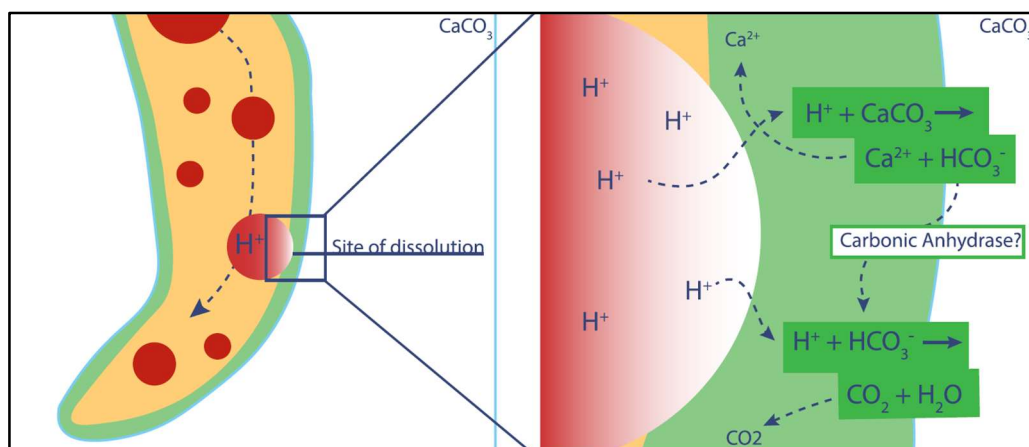


Figure 6: Conceptual model for chemical dissolution of  $CaCO_3$  by excavating sponges [orange; sponge tissue, red; low pH bundles, green; etching interface, white;  $CaCO_3$ ]. Protons are transported via transport cells until

they reach the etching cells. The protons will be integrated into low pH bundles, after which they release their contents. Subsequently, dissolution of calcium carbonate occurs. Over time the etching cells penetrate the carbonate material deeper and deeper due to dissolution. Carbonic anhydrase is hypothesized to speed up the conversion of newly released bicarbonate ions to  $CO_2$ , which then diffuses out of the sponge passively. Figure adapted from Webb et al. (2019).

## 1.6 Relevance

Regarding oyster beds, excavating sponges are considered undesirable from both an economical as ecological point of view. Economically speaking; sponges can infest oyster populations of commercial farms, which is detrimental for the oyster food and pearl industry, because damaged oysters cannot be marketed (Thomas, 1979; Rosell et al., 1999; Rawlinson, 2000; Fromont et al., 2005). Ecologically speaking; boring activity by the sponges leads to weakening of the oyster shells or even mortality. Which can make individuals more prone to predation especially in low-density populations (Thomas, 1979; Pomponi & Meritt, 1990; Rosell et al., 1999).

Another drastic evolution is the disappearance of many oyster beds in the North Sea due to intensive fisheries resulting in the loss of rich hard substrate benthic communities (Bennema et al., 2020). Hence, a lot of research goes into the methods for optimal oyster bank restoration in the North Sea. Research on sponge bioerosion will contribute to the overall knowledge of oyster bed dynamics necessary for successful restoration projects, as the presence of *C. celata* may influence the success potential of such projects.

## 1.7 Research questions

To extend literature on warm water/tropical bioerding sponges, we will test whether excavating sponges would respond similarly to perturbations in inorganic carbon chemistry in cold water environments. Here we will look at the cold water sponge *Cliona celata* present in oyster shells from the Grevelingenmeer and the Oosterschelde in The Netherlands.

So far, the exact mechanism and the belonging dissolution conditions by which sponge bioerosion occurs remain speculative as mentioned earlier and is overlooked in experimental work (de Bakker et al., 2018; Zundeleovich et al., 2007). Mainly due to the etching interface which is not directly accessible for research (Webb et al., 2017). This makes it difficult to analyse bioerosion patterns that arise on carbonate substrates. Here we will be using various microscopy techniques (Fluorescence microscopy & Scanning electron microscopy) which will allow us to take a closer look at this etching interface. This study will contribute to the overall understanding of bioerosion by excavating sponges and will add to the study of Webb et al. (2019), by formulating the following research questions:

- How does bioerosion by *Cliona celata* evolve over time?
- What is the pH during bioerosion and what is the rate of dissolution by *Cliona celata*?

# Methods

## 2.1 Collection, sampling and instalment

Oysters (Japanese oyster: *Crassostrea gigas*) containing alpha-stage *C. celata* were collected from the Grevelingenmeer (Divespot Den Osse: Zeeland, The Netherlands) and the Oosterschelde (Divespot Zeelandbrug: Zeeland, The Netherlands) by SCUBA diving down to a depth of 15m. The oysters were transported to the Royal Netherlands Institute for Sea Research at Texel submerged in seawater in a cooling box. They were placed in open flow-through seawater containers (with a flow rate of approximately  $1.2 \text{ L min}^{-1}$ ) subjected to a natural diurnal light cycle and a constant temperature of  $16^\circ\text{C}$ . Every week, 10 drops of a highly concentrated algae mix (containing *Isochrysis*, *Rhodomonas*, *Tetraselmis* and *Chaetoceros*) was added, as food for *C. celata* (Lynch & Phlips 2000; Wisshak et al., 2014). Water in the aquarium was bubbled with air to keep the water aerated and mix the incoming water with the food.

*C. celata* samples were prepared by fragmenting the oyster shells with a hammer and chisel underwater to expose the sponge tissue within the shells. Using tweezers sponge tissue was carefully removed from the cavities and placed on pieces of Iceland spar (transparent calcite; to mimic natural bioerosion) with an approximate tissue volume of 0.5 ml, similar as in Cobb (1975). The samples were left undisturbed in stagnant water to allow attachment to the Iceland spar (at  $16^\circ\text{C}$ ). After four days, when most sponges attached to the Iceland spar, samples were transferred to a separate flow-through seawater container.

## 2.2 Microscopy analysis

### 2.2.1 Scanning electron microscopy and processing of the images

To analyse the bioerosion patterns on and into the Iceland spar, Scanning Electron Microscopy (SEM) was used. Samples from the flow through containers were retrieved between five days up to around 10 weeks. Sponge tissue was detached from the Iceland spar with tweezers and the pieces were then placed in an ultrasonic bath for 10 minutes in ultrapure milli Q-water to remove most of the remaining sponge tissue on the Iceland spar. They were then left to air-dry before analysis with the SEM. Images were made using a Hitachi TM3030 electron microscope. These images ( $549 \times 549$  pixels) were imported in Python (transformed from RGB to grayscale) as an array where each location in the array represents a pixel from the image with a specific light intensity. By scanning each line in the array horizontally and setting the average of each line equal to the average image intensity a new array was obtained that contained values with per differences from the mean. This removes background scatter and prevents distortion of the image. To make certain bioerosion features pop out even more the contrast of the image was enhanced by adjusting the array values to fit in a range from 0 to 255.

### 2.2.2 Fluorescence microscopy

A fluorescent probe 8-hydroxypyrene-1,3,6-trisulfonic acid (HPTS) was applied to the sponge-spar samples to visualize the pH inside the sponge tissue and at the sponge-calcite interface. HPTS is a weak organic acid with different fluorescent spectra for the protonated and deprotonated form. Since the ratio between these two forms depends on the pH of the medium in which the HPTS is dissolved, the ratio of the fluorescent signals can be used to visualize the pH using fluorescence microscopy. The protonated form of HPTS has its excitation optimum around 405 nm, and the deprotonated form has its excitation optimum around 460 nm; for both forms, the emission optimum lies at 520 nm. The use of HPTS to

visualize the pH has been applied to calcifying foraminifera before. For this study the methods outlined in De Nooijer et al. (2008) were followed by 1) producing a calibration curve to establish the relation between the fluorescence ratio and the pH and 2) application of this calibration curve to sponges incubated with HPTS.

### *Calibration*

A calibration curve was prepared in order to set up a relation between the normalized fluorescence ratio  $\lambda_2^{\text{exc}} / (\lambda_1^{\text{exc}} + \lambda_2^{\text{exc}})$  (with  $\lambda_1=405$  and  $\lambda_2=488$  nm) and the seawater pH. The pH of 25  $\mu\text{M}$  HPTS in filtered seawater was adjusted by adding drops of NaOH or HCl. Images were created using different microscope settings (Pixel time [4, 6 and 7 s], Laser wavelength [0.2 and 0.3 %] and Detector Gain [550, 650 and 750 V]) to check whether changing settings would affect the fluorescence ratio. In order to calculate the ratio between the two excitation optima, pixel intensities with a zero value (i.e. with no fluorescent signal) were removed. The set of calibration scans resulted in the following sigmoidal relation (also referred to as a Boltzmann function):

$$\text{Normalized ratio} \left( \frac{\lambda_2}{\lambda_1 + \lambda_2} \right) = 0.01 + \frac{0.38}{1 + e^{\frac{-(\text{pH} - 6.11)}{0.37}}} \quad (I)$$

The obtained calibration shows that pH can be reliably estimated between  $\sim 5$  and  $\sim 8$  (Figure 7). The curve follows a similar type of relation as in other studies with a HPTS calibration (Weidgans, 2004, de Nooijer et al., 2008). Changing microscope settings yielded a maximum pH offset of 0.06 and could therefore be considered neglectable.

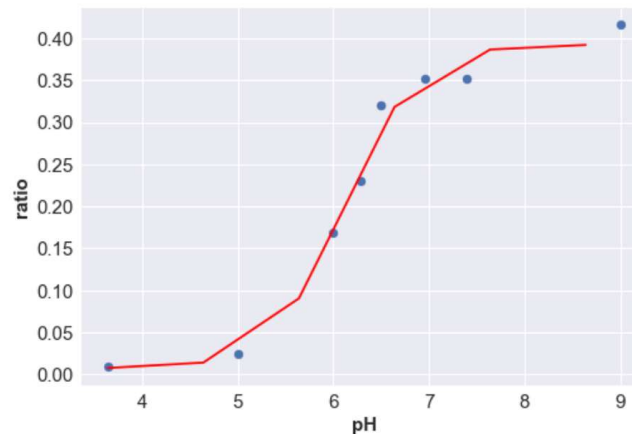


*Figure 7: Radiometric application of HPTS as a function of pH.*

### *Incubation and sample preparation*

In multiple jars filled with filtered seawater solution 25  $\mu\text{M}$  HPTS (pH 7.8 and salinity 30.4 ppt) three sponge-spar samples were placed and incubated at 16 °C for a period between 48h and a week. Following incubation, samples were washed by briefly placing the samples in a beaker with seawater, before examination under the fluorescence microscope.

### *Photographs and processing*

Using a ZEISS LSM 980 confocal laser scanning microscope, HPTS inside the sponge tissue and at the sponge-calcite interface was visualized. Scans were made using the following settings: Pixel time 4 sec, Laser wavelength 0.2 % and Detector Gain 750 V. Two separate tracks were created for each excitation optimum ( $\lambda_1=405$  and  $\lambda_2=488$  nm) and an additional track for a transmitted light background image. Each scan with the fluorescence microscope obtains images for each track separately and a mixed channel image (Figure 8).

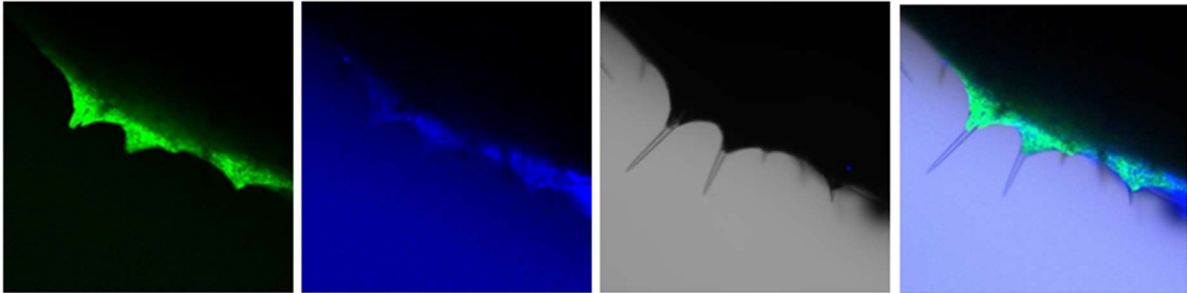


*Figure 8: Output scan fluorescence microscope, from left to right; excitation optimum 1 (405 nm), excitation optimum 2 (488 nm), transmitted light background image, and mixed signal.*

The scans were compressed in one multichannel czi file. To get the original data from the scans the image processing environment of the ZEN3.3 blue software was used. Here separate JPEG images for each excitation track and the light background could be retrieved in gray RGB format (Figure 9). These images were imported in Python and transformed to true grayscale for further analysis.

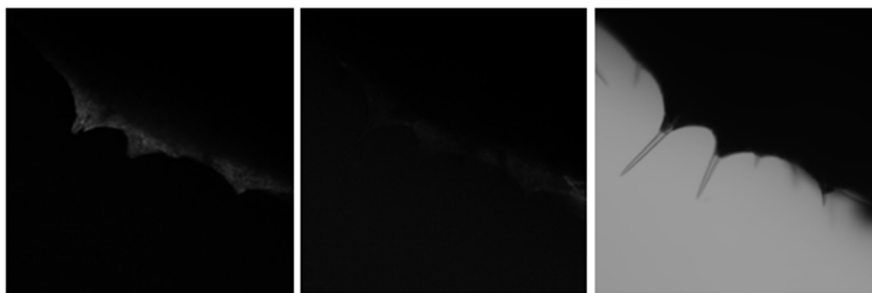


*Figure 9: Original raw data fluorescence microscope (GRB grayscale), from left to right; excitation optimum 1 (405 nm), excitation optimum 2 (488 nm), transmitted light background image.*

### *Python*

Scan images obtained by the fluorescence microscope were imported in python which allowed making calculations and creating pH maps. To do so images were imported in grayscale format and transformed into 2D arrays where each location in the array represents a corresponding pixel light intensity of the

grayscale image. The normalized ratio between the two excitation optima images was calculated and with the calibration curve (Figure 7) converted to a pH array.

For the calibration curve the average normalized ratio was used by taking the average of all pixel ratios. This was plotted against the known pH of the prepared solution, Figure 7. For the analysis of the sponge-spar samples, the normalized ratio was again calculated for all pixels and stored in a new array. This array was transformed using the sigmoidal calibration (Formula I) and subsequently plotted as an image and overlain over the non-fluorescent light background image (with same dimensions) which was taken simultaneously with the fluorescence images.

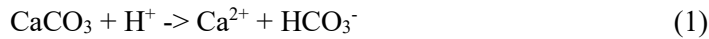
For the complete python code on how the pH maps were created see Appendix A.

### *Software*

For the development and analysis of the pH maps different software programs were used. As mentioned before, the image processing environment of the ZEN3.3 blue was used to obtain the original raw data of the fluorescence microscope scans. Python (version 3) was used to develop the pH maps. And ImageJ (Fiji) was used to analyse the pH bundles from the Python pH maps.

### *Local flux*

From the python pH maps the local proton flux in the sponge tissue was calculated. This was done by taking a transect in the pH maps, which yielded information regarding the proton concentration over distance. Using the principles of Toyofuku et al. (2017) for foraminifera the local flux at the sponge edge was determined. It was assumed that protons eventually get released from the sponge and diffuse around with some of them being consumed in the reactions with calcium carbonate from the Iceland spar and bicarbonate released from that reaction:



Using these assumptions the proton concentration around the sponge tissue can be approached by the diffusion equation with consumption:

$$\frac{\partial}{\partial t} [\text{H}^+] = D_H \nabla^2 [\text{H}^+] - \mu ([\text{H}^+] - [\text{H}^+]_{\infty}) \quad (\text{IV})$$

$D_H$  is the diffusion coefficient of protons  $D_H = 9.3 \times 10^{-5} \text{ cm}^2 \text{ s}^{-1}$ ,  $\nabla^2$  is the Laplacian operator and  $\mu$  is a combination of the constant rate of the reactions with calcium carbonate and bicarbonate. Using boundary conditions;  $[\text{H}^+] = [\text{H}^+]_{\infty}$  at  $r \rightarrow \infty$  and  $[\text{H}^+] = [\text{H}^+]_R$  at  $r = R$ , equation IV can be solved.  $[\text{H}^+]_{\infty}$  is in this case the equilibrium proton concentration in the sponge tissue and  $[\text{H}^+]_R$  is controlled by the sponge. When the sponge starts to release its etching agent,  $[\text{H}^+]_R$  increases and eventually becomes larger than  $[\text{H}^+]_{\infty}$ . After a period of time, equilibrium has been reached, and the spatial distribution of protons follows the steady solution of equation IV and is represented by:

$$[\text{H}^+] = \alpha \frac{K_{1/2}(kr)}{(kr)^{1/2}} + [\text{H}^+]_{\infty} \quad (\text{V})$$

In this equation  $K_{1/2}$  represents the second type of the modified Bessel function  $K_a$  with  $a = 1/2$ , and:

$$k \equiv \sqrt{\frac{\mu}{D_H}} \quad (\text{VI})$$

The Non-linear Least Squares fitting of the transect data with equation V was used to estimate the values of the parameters;  $\alpha$ ,  $k$ ,  $[H^+]_\infty$ . From  $k$  and equation VI,  $\mu$  could be determined. From the fitted curve the proton gradient at the sponge edge could be determined which together with the  $D_H$  can be used to calculate the local proton flux:

$$J_R = -D_H \left( \frac{\partial [H^+]}{\partial r} \right)_{r=R} \quad (\text{V})$$

## Results

### 3.1 Scanning electron microscope images

First marks of bioerosion appeared as small holes that were organized in various configurations (Figure 10a). These holes could already be encountered after approximately five days. This coincides with the moment most aggregates of sponge tissue attached to the Iceland spar. After approximately a week, more channel like and random shaped bioerosion features appeared on the spar surface. Some of these channels follow a certain ‘preferential’ direction (Figure 10b). In contrast, other channels have a completely irregular character (Figure 10c).

.....

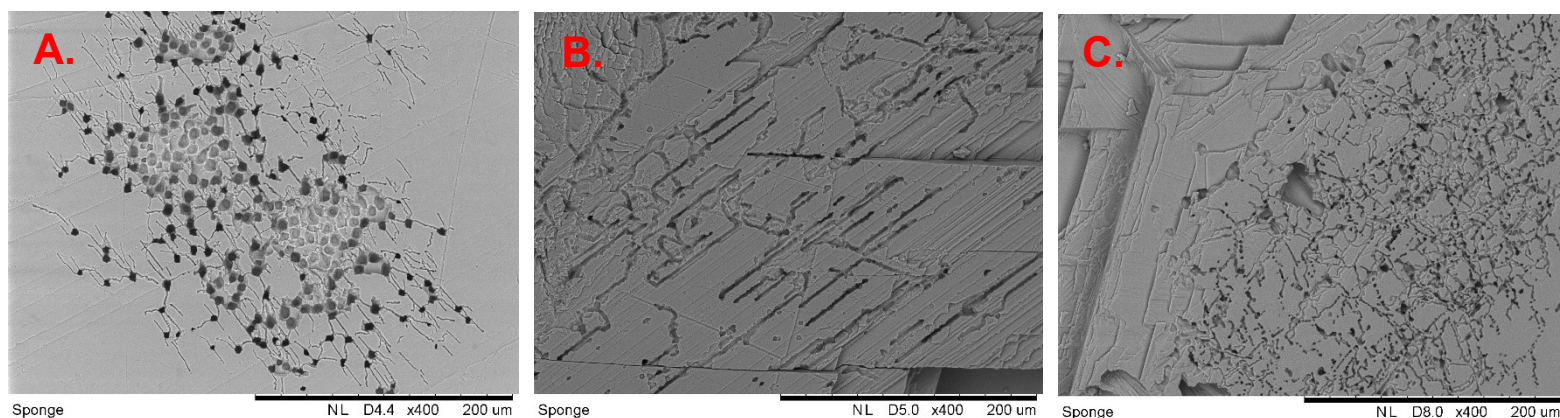


*Figure 10: SEM images initial stage bioerosion: (a) Magnification 400x. (b) Magnification 400x. (c) Magnification 400x.*

.....

After approximately four to five weeks other *C. celata* bioerosion marks appeared. Initial etching shows up as elliptical/curvilinear shaped etching marks on the Iceland spar surface (Figure 11b&c). These etchings appear as crevices with an irregular wavy characteristic that in shape seem to follow the cell edge of the etching cells. These crevices over time become deeper and deeper which together with chip removal leads to the formation of cone shaped depression (pits), with an approximated average depth

of 22  $\mu\text{m}$  (Appendix B). These pits are connected to each other but are separated by distinct ridges. In some of the pits hemispherical chips (approximately 55  $\mu\text{m}$ ) are still visible, Figure 11a-c. The chips have sharp corners with flat surfaces. A closer look at the pit walls and chip surfaces reveal a type of micro layering with separated terraces (Figure 11a,c&d). See Appendix B, for a calculation about the eroded volume of Figure 10b.

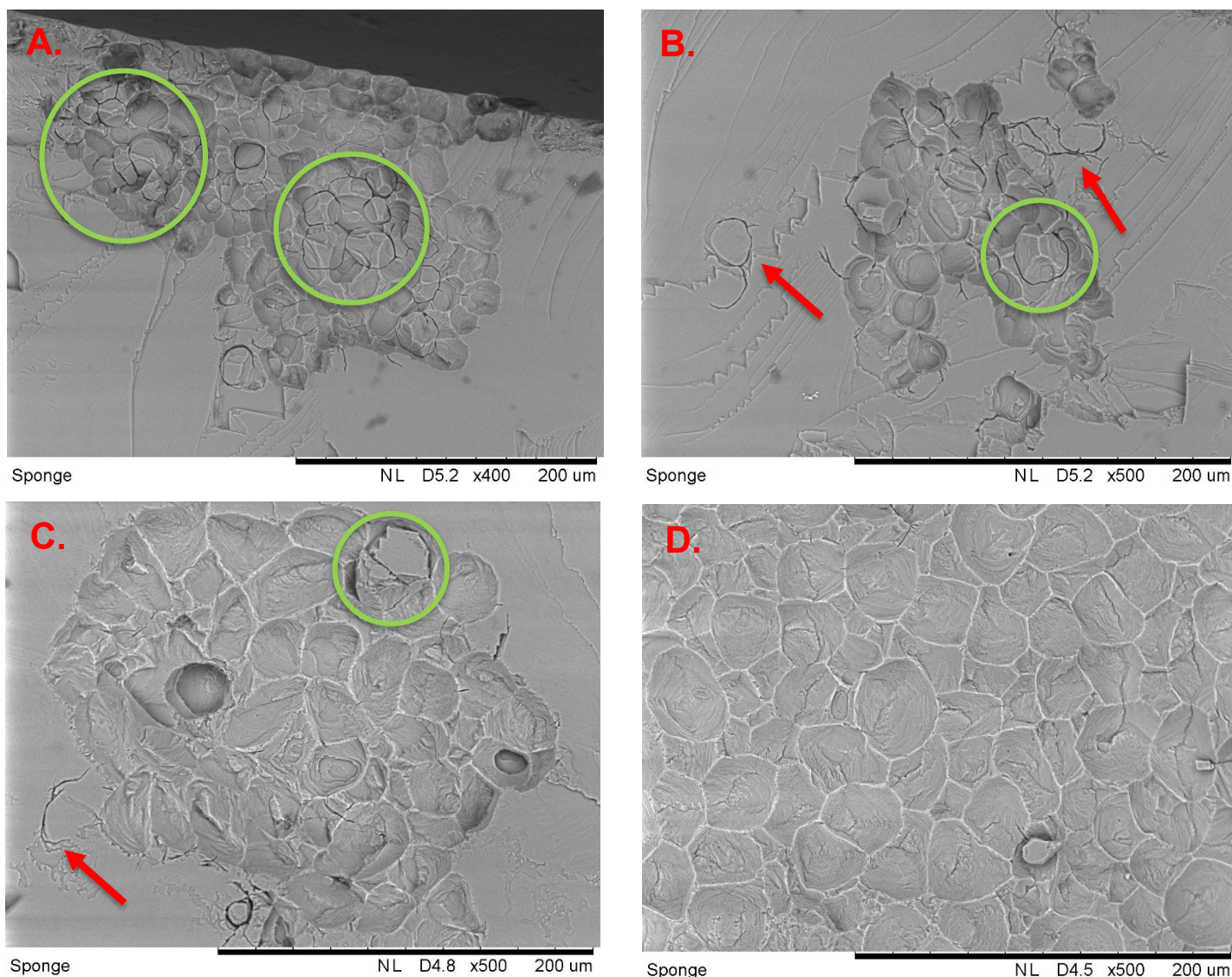


Figure 11: SEM images showing etching marks (red arrows), pits and chips (green circles): (a) Magnification 400x. (b) Magnification 500x. (c) Magnification 500x. (d) Magnification 500x.

After about six to seven weeks pitted holes start to form (Figure 12). These holes are a result of penetration by the sponge in the Iceland spar and form the starting point for tunnel formation. The holes in Figure 12a. show variety in shape and dimensions, with diameters ranging between  $\sim 0.04$  mm and  $\sim 0.3$  mm. Some of these holes start to connect to each other to form larger holes (Figure 12b).

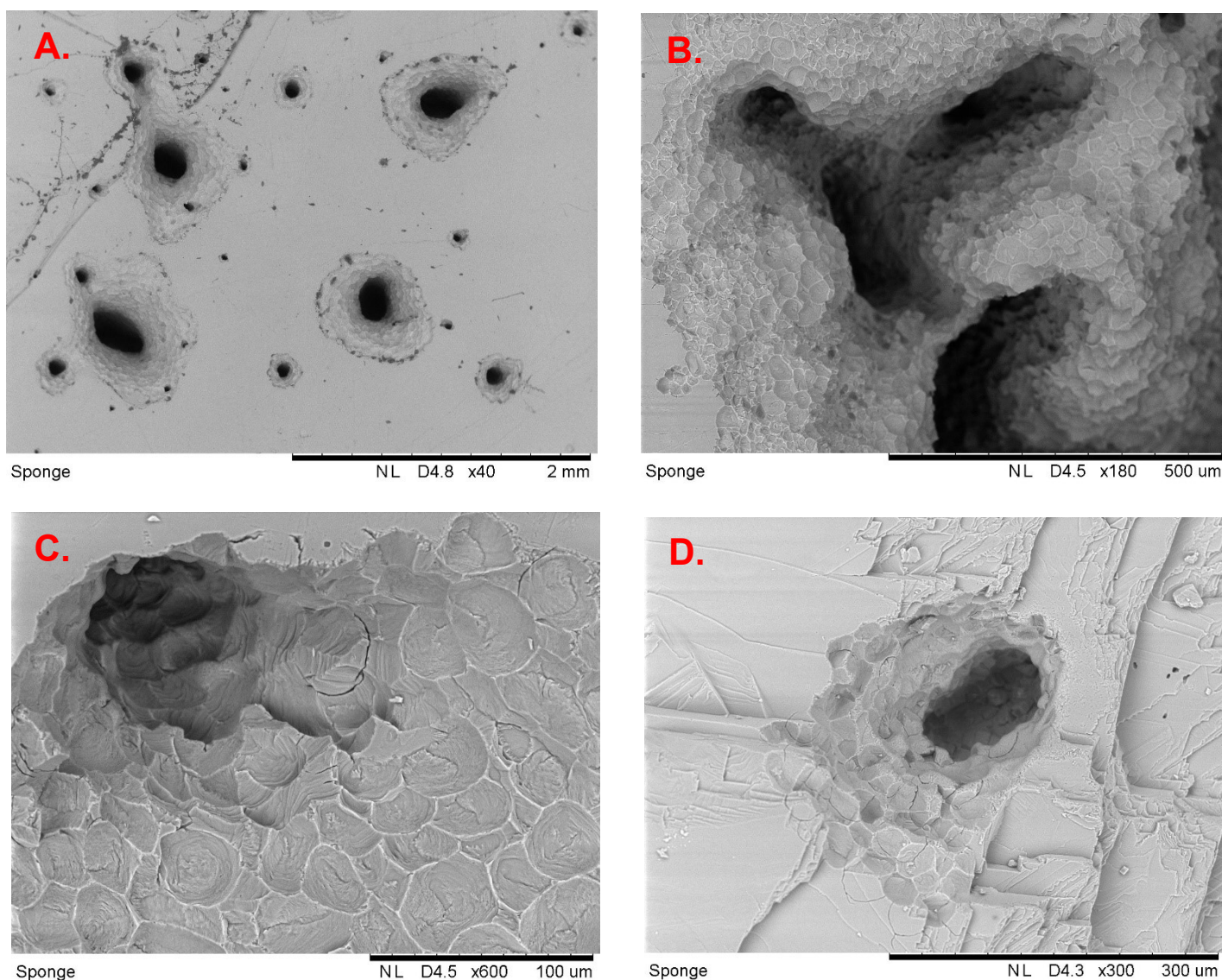


Figure 12: SEM images pitted holes: (a) Magnification 40x. (b) Magnification 180x. (c) Magnification 600x. (d) Magnification 300x.

Around 10 weeks, penetration of the sponge in the Iceland spar became also visible by eye. This resulted in larger and more irregular bioerosion features (Figure 13; compare with the magnification of Figures 11 and 12). More and more pitted holes started to connect to each other to form bigger tunnels inside the Iceland spar. Because the tunnels were deepening, it was difficult to remove all the organic material inside these tunnels with the ultrasonic bath (Figure 12a&c). This explains the spicules (structural elements present in sponges) and other single-celled material visible in the tunnels. Most of the Iceland spar surface show pit marks, which means that bioerosion started to take place at a larger scale. Overall, we see that we can distinguish different bioerosion phases over time that ultimately lead to penetration of the sponge into the Iceland spar (Figure 14).

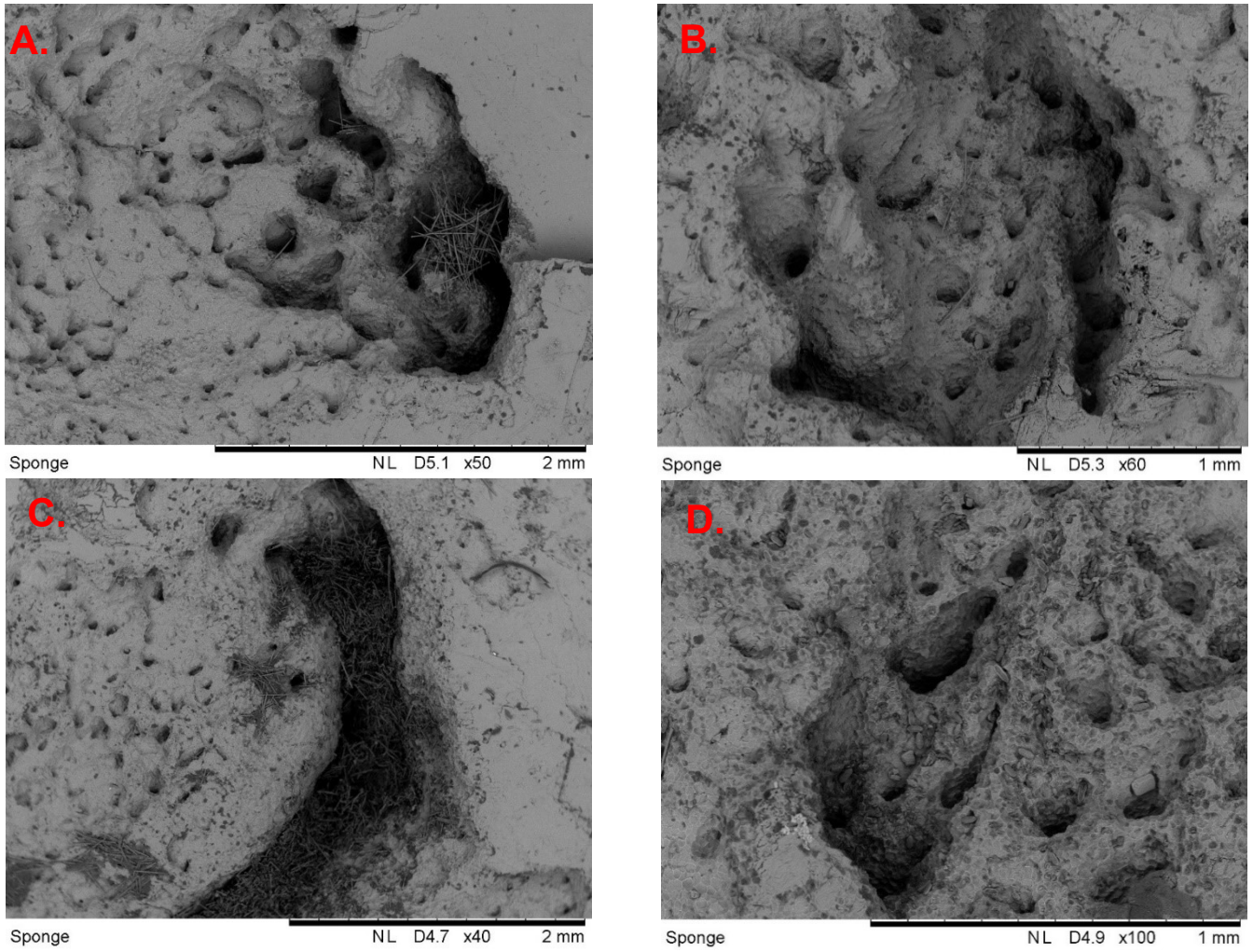


Figure 13: SEM images pitted tunnels: (a) Magnification 50x. (b) Magnification 60x. (c) Magnification 40x. (d) Magnification 100x.

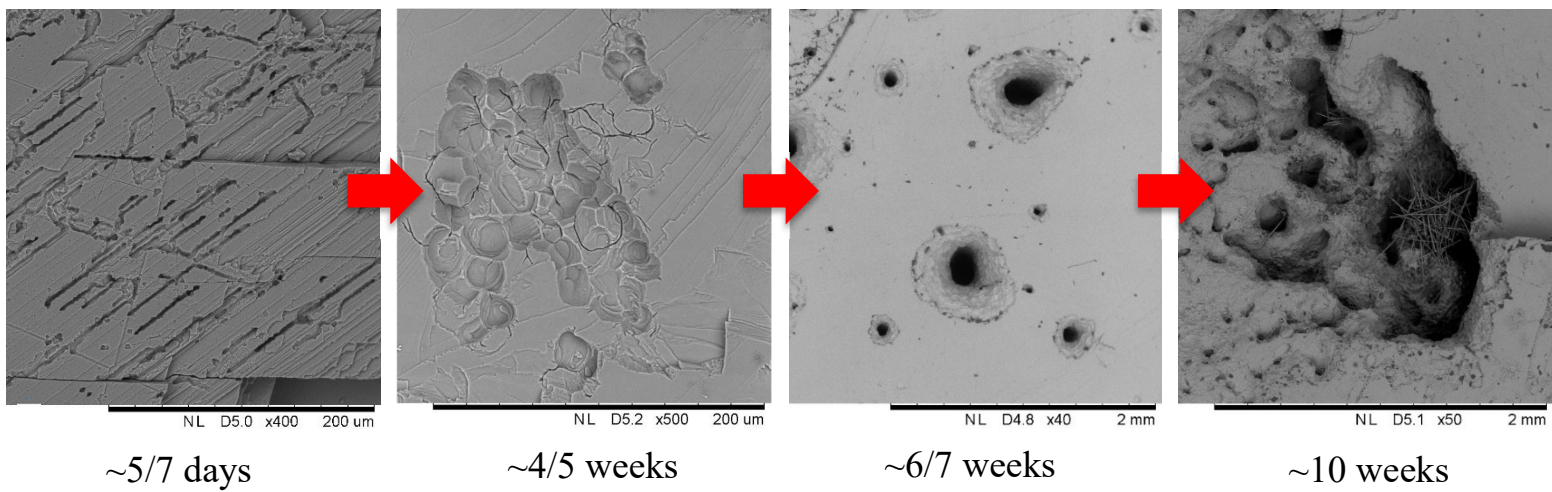


Figure 14: Timeline erosion development *C. celata* on Iceland spar.

### 3.2 Fluorescence microscope images

Visualization of HPTS reveals a pH reduction at the sponge-spar interface. This relatively low pH is apparent from spherical to irregular-shaped intracellular bodies (Figure 15). The pH in these ‘bodies’ varies around 6, with extremes ranging from 3.3 to 8.3. Image A. shows a large stroke of a lower pH region at the outgrowth of the sponge tissue with an approximate surface area of  $\sim 1200 \mu\text{m}^2$ , there are also smaller bundles present with a varying size between  $\sim 500$  and  $\sim 50 \mu\text{m}^2$ . A sponge spicule can be seen on top of the Iceland spar. The pH bundles in images B-F. are all fairly similar in size approximately  $\sim 5 \mu\text{m}^2$ . Image G. shows two larger lower pH regions with an approximate area of  $\sim 3500 \mu\text{m}^2$ . In image H. a gradient in pH is visible with lower values near the Iceland spar and higher values more inward of the sponge tissue, from this image a local flux is estimated (see section 3.3).

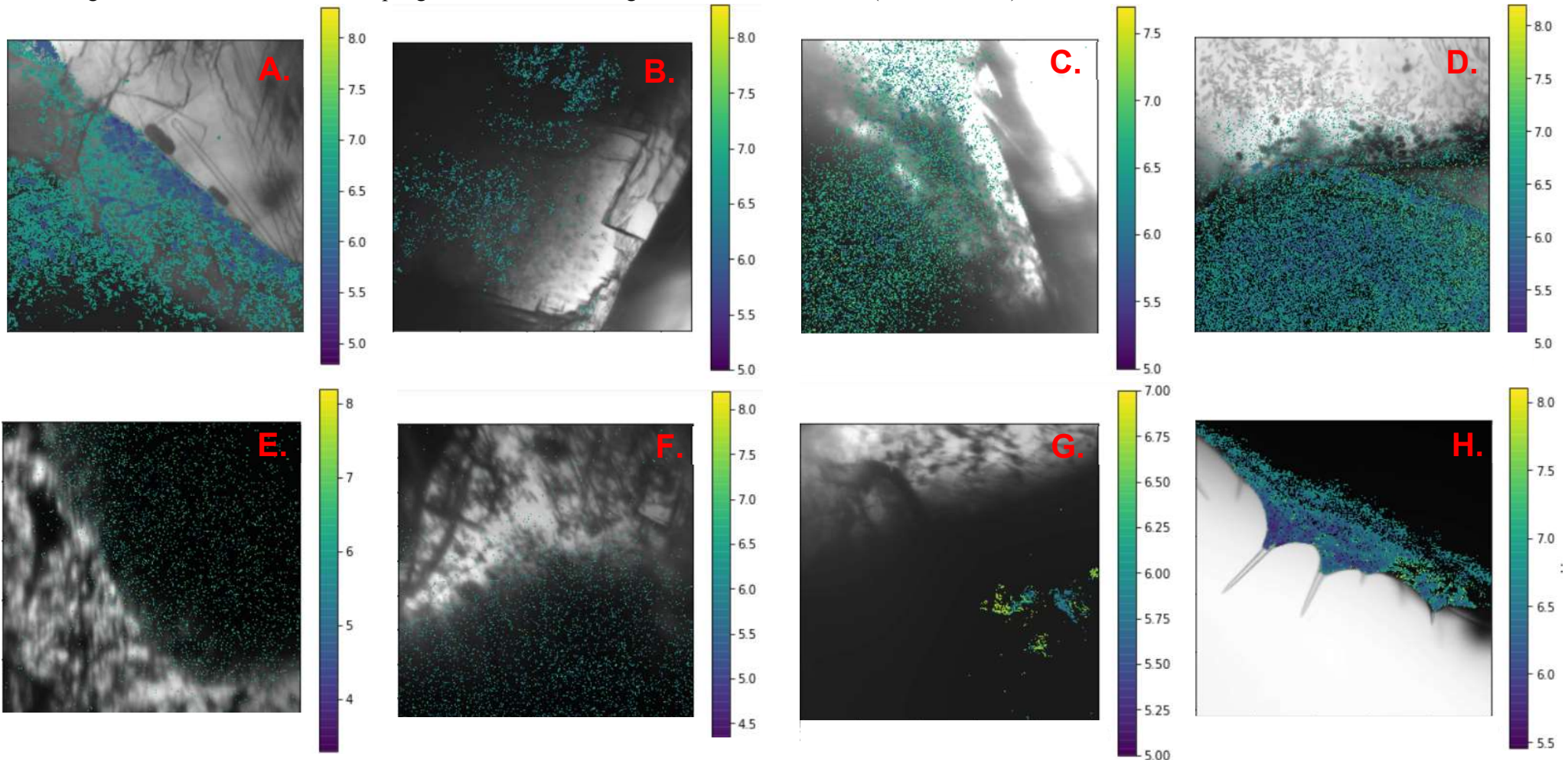


Figure 15: Low pH bodies at sponge-Iceland spar interface (sponge tissue; dark, Iceland spar; light). All images were scanned using magnification 5x but were cropped: (a) 357x357  $\mu\text{m}$ . (b) 880 x 880  $\mu\text{m}$ . (c) 849 x 849  $\mu\text{m}$ . (d) 576 x 576  $\mu\text{m}$ . (e) 988 x 988  $\mu\text{m}$ . (f) 976 x 976  $\mu\text{m}$ . (g) 849 x 849  $\mu\text{m}$ . (h) 355x355  $\mu\text{m}$ .

### 3.3 Local flux

Figure 16 shows an example for the relation of proton concentration (calculated from the pH) with distance. An transect was drawn from the sponge-calcite interface (lower pH) towards the inner sponge tissue (higher pH). The proton concentration decreases until approximately  $\sim 68 \mu\text{m}$  after which a more or less stable plateau concentration is reached. Striking is the sharp increase in proton concentration near the sponge-calcite interface (Figure 16b). In order to calculate the local proton flux at the sponge edge, this increase in proton concentration was discarded. What remains is a ramping or the proton concentration over distance in which the final plateau level was extended to compensate for the discarded data points. Figure 16c shows the adjusted data with the fitted steady solution of the diffusion-consumption equation (V), with parameters;  $\alpha$  ( $4.3 \times 10^{-11}$ ),  $k$  ( $0.017 \text{ cm}^{1/2} \text{ mol}^{-1/2}$ ),  $[\text{H}^+]_{\infty}$  ( $4.6 \times 10^{-7} \text{ mol L}^{-1}$ ), and  $\mu$  ( $2.6 \times 10^{-14} \text{ L mol}^{-1} \text{ s}^{-1}$ ). The proton gradient was calculated at the starting point of this curve:  $-3.25 \times 10^{-7} \text{ M } \mu\text{m}^{-1}$ . This results in a local proton flux of  $3.02 \times 10^{-8} \text{ mol dm}^{-2} \text{ s}^{-1}$  for this transect. See Appendix C for more proton concentration transects.

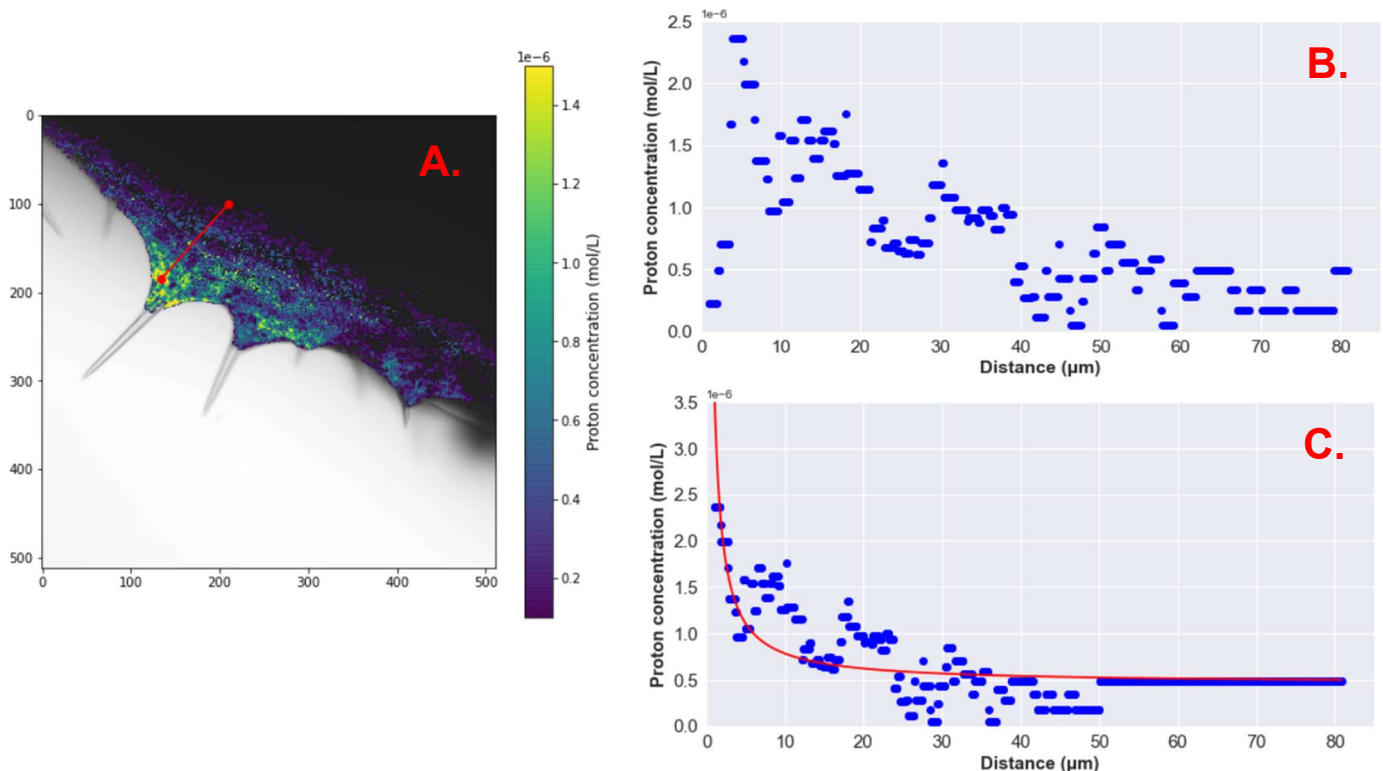


Figure 16: (a) Transect proton concentration. (b) Proton concentration plotted over transect distance. (c) Proton concentration plotted over transect distance with first data points discarded and extended final plateau level. Red fitted curve for the steady state solution of the diffusion equation with added consumption.

# Discussion

## 4.1 Scanning electron microscope images

The stages in bioerosion patterns found here (Figures 11-13) are in line with those described before (Cobb., 1969). Initially the sponge tissue with specialized etching cells (amoebocytes) flattens out over the calcite surface. The cells that are in contact with the Iceland spar release an acidic etching agent which dissolves the calcium carbonate of the spar around the edge of the cell. This is also seen in the curvilinear crevices that correspond in size and shape to the contours of the cell (Figure 11b&c). Over time etching activity by these cells may form more complex patterns. The first stage of the crevices appears as narrow, shallow grooves but become deep undercuts as bioerosion proceeds. Due to continuous undercutting chips of calcium carbonate are removed from the substratum and leave behind a field of conical-shaped depressions (pits; Figure 12). These chips are mechanically transported out of the sponge tissue through the mesenchyme followed by transport through the excurrent water canals to the oscula. (Cobb, 1969; Topsent, 1887). This undercutting is due to the cell edge that slowly dissolves its way into the Iceland spar. At the location where the cell edge penetrates the Iceland spar, a thin layer of calcium carbonate gets continuously dissolved until a chip is removed and a complete pit is formed. The pit walls and chip surfaces showed an irregular, micro layered topography (Figure 11a,c&d). According to Cobb (1975) this is an indication for a localized control of dissolution. As the concentric microlayers decrease in diameter getting deeper in the pits Cobb (1975) concluded that bioerosion by *C. celata* occurs in a step-like fashion where the cell edge penetrates in the carbonate substratum gradually constricting in circumference as it undercuts the Iceland spar. When time progresses the sponge gradually erodes deeper into the Iceland spar and forms pitted holes which eventually may become a network of chambers and tunnels (Figure 13).

An important caveat to these results should be that Iceland spar does not necessarily have the same physical properties as oyster shells. This could possibly influence the bioerosion patterns that arise. However, according to Cobb (1975), fine structural bioerosion features are similar for Iceland spar and shell material, even though the crystal morphology differs. Iceland spar is a pure form of crystalline calcium carbonate whereas mollusc shell substratum is both chemically and structurally heterogeneous. Calcified mollusc shell layers consist of calcium carbonate crystals which are surrounded by envelopes of an organic intercrystalline matrix of conchiolin (Grégoire, 1961; Watabe, 1963) and divided into sub compartments by an intracrystalline matrix (Watabe, 1965). Only some slight differences were reported but the mechanism of cellular penetration was not selectively influenced by the organic-crystalline composition of the substratum. The main difference in bioerosion between Iceland spar and oyster shell has to do with the micro-layered structure present on the pit walls and the chip surfaces. These appear smoother on Iceland spar compared to oyster shell substratum and might indicate a difference in solubility between the organic matrix and crystalline calcium carbonate (Cobb, 1975).

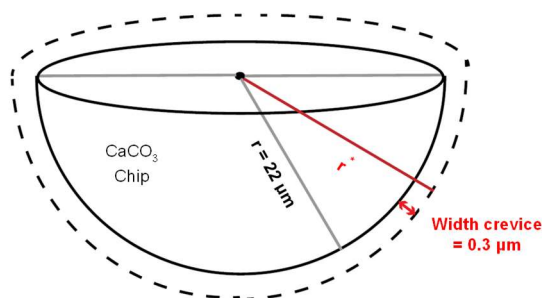
This study also revealed bioerosion features not described before. Prior to the formation of crevices, features appeared on the Iceland spar (such as holes and both regular and irregular shaped channels) with similar dimensions as etching marks and pits (see Figure 10). A possible explanation for these more unexpected patterns might be because of the surface morphology and crystallization of the Iceland spar. Dissolution of Iceland spar depends on the initial surface morphology (Compton et al., 1986). For example, a surface with a higher roughness enhances dissolution. This was also seen during this study; some initial scratches on the Iceland spar surface made the sponge attach faster and led to earlier bioerosion marks. Newly cleaved Iceland spar pieces tend to be 'unreactive', but as time proceeds the

spar surface roughness increases due to dissolution. This is interesting since Iceland spar pieces for this study were created by hammering larger blocks of Iceland spar into smaller pieces, which creates a new cleaved surface. So, initially dissolution by *C. celata* might be low because of the freshly created spar surface. However, this was not tested in this study. Additionally, the crystal lattice of Iceland spar may contain misorientations or micro-flaws which can make certain locations in the spar more sensitive to dissolution (Bjornerud, 2007). For example, microcracks or dislocations present in the crystal (lattice) can make the crystal weaker. Dislocations are places where something has gone wrong building up atoms in lattice. Remarkable is that the channels in Figure 10b, indeed seem to follow the direction of the lattice layers. But other than that, there is no real evidence found in this study that these more unexpected patterns may arise from initial surface morphology or crystallization flaws of the Iceland spar. One way that might help understanding these patterns is to work with a transmission electron microscope which can be used with intact sponge- spar samples to study the spatial relationship between the etching cells and the crystal organization (Cobb, 1975).

## 4.2 Fluorescence microscope

This is one of the first studies to provide evidence that acid production plays a role in bioerosion by excavating sponges in an experimental setting, by spatial visualization of the intracellular sponge pH. Previous attempts to detect acid in excavating sponges mostly failed due to insufficient sensitivity of the techniques utilized (Schönberg, 2008). Here, we showed that the use of a fluorescence probe is a successful method to detect intracellular low pH bundles. To date, This technique has only been successfully applied once before on samples of *Cliona varians* by Webb et al. (2019). Cobb (1969) and Hatch (1980) suggested that bioerosion by *C. celata* is initiated due to dissolution of calcium carbonate by locally lowering the pH. The low pH bodies in the images from Figure 15 seem to confirm this theory. They show lower pH bundles present at the edge of the sponge tissue with the Iceland spar. In some of the pH maps the intracellular pH decreases towards the Iceland spar (Figure 15 A, D & H). This is in line with the study by Schönberg (2008) where using microsensors a continuous decrease of pH was observed towards the substrate for *C. celata*. It is likely to assume that at these spots bioerosion takes place, because the creation of an acidic microenvironment would lead to a change in the carbonate solubility equilibrium, favourable for dissolution.

The pH maps in Figure 15 reveal an average pH ~6 in the low pH bundles. Together with an estimated volume of such a bundle we can calculate the number of protons present inside a bundle, which then can be translated to the maximum volume of calcium carbonate that can be dissolved (Figure 17). Assume that chips can be approximated by a hemispherical shape, similar as in Webb et al. (2019). These chips have a diameter of around 44  $\mu\text{m}$  (Average observed pits; Figure 11 and Appendix B). The width in which the cell edge of the etching cells subsides is approximately 0.2  $\mu\text{m}$  (Crevice width Figure 11). Based on this information and the approach by Webb et al. (2019) we estimated that approximately  $2.50 \times 10^{-11}$  mol  $\text{CaCO}_3$  dissolves for each chip that is removed by *C. celata*, which means that around 4% of the eroded material dissolves. This is in line with what is found in previous studies and shows the proportion between chemical and mechanical bioerosion by *C. celata*. According to Warburton (1958) less than 10% of the total amount of calcium carbonate removed by *C. celata* gets dissolved. Rützler and Riegler (1973) made a similar estimation for the excavation sponge *Cliona lampa* and found that around 2-3% of the eroded material gets dissolved.



$$V_{whole} = \left(\frac{4}{3}\pi r^3\right)/2$$

$$V_{chip} = \left(\frac{4}{3}\pi r'^3\right)/2$$

$$V_{dc} = V_{whole} - V_{chip}$$

$$M_{gram} = \rho \times V_{dc}$$

$$[CaCO_3] = M_{gram} / W_{molar}$$

Figure 17: Schematic representation of calcite chip.  $V_{whole}$  is combined volume of chip and volume dissolved  $CaCO_3$ ,  $V_{chip}$  is chip volume,  $V_{dc}$  is volume of dissolved  $CaCO_3$ ,  $M_{gram}$  is mass of  $CaCO_3$  dissolved,  $\rho$  is density of Iceland spar and  $W_{molar}$  is molecular mass of  $CaCO_3$ . Figure adapted from Webb et al. (2019).

The proton concentration  $[H^+]$  in the bundles with a pH 6 is equal to  $10^{-6}$  mol/L. If we assume that the crevice undercut is entirely taken up by low pH bundles we can calculate the amount of bundles that fit in this region. Regarding Figures 15 B-F we assume that one bundle has an approximate volume of  $\sim 6.56 \mu m^3$ . This means that around 141 bundles fit in this undercut region, which in total leads to  $9.25 \times 10^{-19}$  mol protons in this region at one time. This is more than an order of magnitude lower compared to Webb et al. (2019) where a similar calculation was made for *Cliona varians*. The offset between these results could be explained by the much smaller size recorded for low pH bundles in *C. varians* ( $0.01 \mu m^3$ ). It might be that different excavating sponge species produce different sizes of low pH bundles, but this requires further research.

Most likely the number of protons found in this undercut region is estimated too high for both this study and Webb et al. (2019). Both studies assumed that the entire undercut crevice is filled with low pH bundles, which probably is an overestimation of the actual amount of bundles present in this region. To make a more reliable estimation further research is required at this etching interface, which is complicated as this interface is not directly accessible and asks for fine scale investigation.

In reality, this calculation will also get even more complicated. Protons released by the sponge in the low pH bundles diffuse around until they react with other chemical components. The protons will initially mostly react with the calcium carbonate present in the Iceland spar, but as time proceeds more and more bicarbonate will be released during this dissolution reaction. The bicarbonate will eventually neutralize some of the protons (Reaction 1 and 2). This means that active proton pumping by the sponge is required in order to keep the pH continuously lowered at the etching sites. We estimated a local proton flux of  $3.02 \times 10^{-8} \text{ mol dm}^{-2} \text{ s}^{-1}$  (Figure 16). If we would use this flux and assume that the neutralization reaction with bicarbonate can be neglected, and all protons are taken up in the dissolution reaction with  $CaCO_3$ , we get a local chemical erosion rate for *C. celata* of  $\sim 0.11 \text{ mg cm}^{-2} \text{ h}^{-1}$ . This seems to be an order of magnitude too high compared to other studies with excavating sponges (Duckworth & Peterson, 2013; Table 1 in de Bakker et al., 2018). However, direct comparison with other studies is difficult because of differences in experimental methodologies and environmental variables used. Most studies use natural substrates to determine a total chemical bioerosion rate and derive this rate from change in alkalinity in flow-through incubation or change of substrate weight. Whereas, this study used Iceland spar as erosion substrate and the rate is locally determined from modelling a proton transect with a form of the linear Heat-Diffusion equation with many underlying assumptions.

## 4.3 Recommendations and Limitations

### 4.3.1 Materials

In order to obtain high resolution fluorescence scans it is preferable to have very thin pieces of Iceland spar as light needs to penetrate through the spar. In this study small pieces of Iceland spar were created by hammering larger pieces. However, this resulted in cracks inside the spar (Figure 15 A, B & F). To prevent this an attempt was made to work with a laser drill, but the spar pieces were too brittle and broke apart easily. Therefore, we would recommend if small pieces of Iceland spar could be purchased from the start.

### 4.3.2 Sample preparation

Several methods have been tried to get the sponge to attach to the Iceland spar. For the first attempt, sponge tissue was collected from fragmented oyster shells with tweezers and then placed on a piece of Iceland spar topped with a mesh secured with an elastic rubber band. But after being placed back in the flow-through containers for about four days, the sponge turned from bright orange to dark brown and on some of them a type of white fungus appeared (Figure 18a). As an alternative approach Iceland spar pieces were directly placed against fragmented shell pieces containing *C. celata* with fishing rope or smaller elastic bands (Figure 18b). However, this method was also unsuccessful as largely no sponge attached to the Iceland spar pieces. After a conversation with sponge expert Alice Webb small inundations on the Iceland spar were created by making raster-like scratches and holes with a knife. This makes it easier for the sponge to find a location to attach. The Iceland spar pieces were later repositioned against fragmented oyster shell pieces with *C. celata*. This approach was more successful, but could not be used for the analysis with the fluorescence microscope as the shell material did not allow light penetration. To circumvent this, small pieces of Iceland spar were pushed inside tunnels containing a lot of sponge tissue (Figure 18c) and later on removed together with the surrounding tissue. However, it was difficult to see whether the sponge attached to the Iceland spar. Finally, we were able to find a successful method where *C. celata* attached to the Iceland spar and which could also be used for the fluorescence microscope. Following a similar approach as in Cobb (1975), sponge tissue was again collected from fragmented oyster shells and clusters of sponge tissue were placed on top of Iceland spar pieces in a jar containing stagnant seawater. After a couple of days these clusters started to clump together and form small spheres fully attached to the Iceland spar (Figure 18d). At this moment the samples were transferred to a seawater flow-through container. We would recommend to use this final approach for further studies with *C. celata* and Iceland spar.

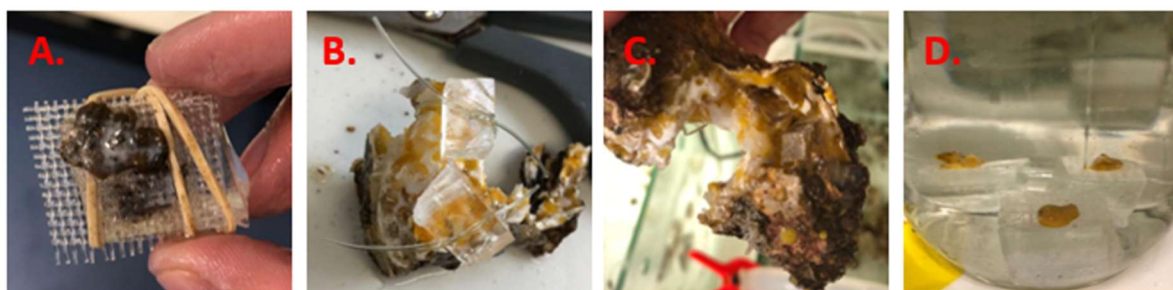


Figure 18: Sponge-spar attachment.

### 4.3.3 Calibration

The prepared HPTS pH solutions were very sensitive to pH change. Even when the solutions were stored in individual sealed tubes in a dark place, the pH of the solutions changed rapidly. Initially, a series of solutions with pH values ranging from 3.5 to 9 were prepared. However, the pH of these solutions changed to pH ~8 after only one day (corresponding to the pH of seawater). We recommend for future HPTS calibrations to prepare each pH solution separately, and take all scans at the different microscope settings immediately after the solution is prepared. This would minimize the change in pH.

Due to time constraints we were unable to prepare duplicates for the calibration. To get a more reliable calibration curve, it is recommended to make duplicates or even triplicates of each pH solution and in addition have some other randomly prepared pH solutions to see if they would fit the calibration curve.

The obtained calibration showed us that the pH could be reliably reconstructed between 5 and 8 (Figure 7). However, the pH in the images from Figure 15 contained extremes ranging from 3.3 to 8.3 (in which 8.3 is likely the seawater pH). In order to analyse the extremes, it is recommended to use a different fluorescent probe, because uncertainty may arise using HPTS.

### 4.3.4 Microscopy analysis

As mentioned before, the SEM images from Figures 11-14 reveal distinct bioerosion phases. It would be interesting for a follow-up study to relate the erosion development phase to the amount and locations of low pH bundles present. This would also result in a more reliable estimation for the proton flux over time. However, this would require an alternative ‘non-destructive’ approach compared to the method used in this study. To use SEM for erosion phase analyses, the sponge tissue must be completely removed. This makes it difficult to locate the same spots with the fluorescence microscope and the scanning electron microscope.

Although the results from the fluorescence microscope reveal intracellular acid production and potential bioerosion spots, it also has its limitations. With fluorescence microscopy it is still not possible to determine the composition of the etching agent responsible for lowering the pH at the sponge-calcite calcite interface. It is also difficult to predict and examine exact spots of bioerosion without damaging or removing sponge tissue. The low pH bundles from the maps in Figure 15 indicate potential bioerosion sites, but this cannot be said with absolute certainty as the maps are only snapshots. In order to see whether actual bioerosion takes place, taking snapshots or a video over time would be recommended.

### 4.3.5 Flux calculation

The method used in this study to calculate the proton flux still requires improvement. Among the proton concentration transects much variation exists (Appendix C), which made it impossible to calculate a flux for all transects. This method is based on foraminifera, which are more perfectly spherical shaped homogeneous organisms. Whereas, the sponge tissue has a more heterogeneous and irregular character, which explains the variation in transects between and within individuals and why the protons are much more irregularly distributed.

Another discussion point are the data points that were discarded in Figure 16c to fit the diffusion curve. One can see that the proton concentration increases sharply in the beginning and then decreases, Figure 16b. This increase was ignored for the flux calculation. However, this peak may indicate that protons are actively being sucked towards this point from multiple directions. Therefore, to calculate a more reliable proton flux, we recommend developing a 3D diffusion model in which transects can be drawn in multiple directions.

#### 4.4 Future state of excavating sponges

It is expected that the impact of excavating sponges will become even more prominent in the future (Kennedy et al., 2013; Perry et al., 2014). Various studies have shown increasing boring activity with higher expected seawater  $p\text{CO}_2$  levels in future climate scenarios (Wisshak et al., 2012; Webb et al., 2017). Elevated seawater  $p\text{CO}_2$  levels result in ocean acidification and thereby lowers the  $\text{CaCO}_3$  saturation state. This means that less energy from the sponge is required to create an acidic microenvironment during dissolution (Webb et al., 2019). Wisshak et al. (2014) predicted that bioerosion rates by *C. celata*, for example, will increase more than double with ocean  $p\text{CO}_2$  levels predicted for the end of this century.

The effect of global warming on excavating sponges is a bit more complicated. For Symbiodinium-containing sponges, bioerosion rates will decrease with higher seawater temperatures because it disrupts the microbiome system and can even cause bleaching of the sponge above certain threshold temperatures (Hill et al., 2016; Achlatis et al., 2017; Ramsby et al., 2018a, 2018b). However, according to Duckworth and Peterson (2013), higher seawater temperatures will have little effect on sponge growth, survival and boring activity of *C. celata*.

Organic pollution (eutrophication: release of nutrients, organic run-offs and poorly treated wastewater discharge in surface waters) has proven to further enhance the pressure on carbonate systems. Eutrophication may lead to elevated  $p\text{CO}_2$  levels in the system which will stimulate boring activity (Gast et al., 1999; Govers et al., 2014). It can also cause a shift in the benthic community where opportunistic organisms, such as the excavating sponges, can benefit from changing conditions and eventually disrupt the system (Holmes, 2000; De Bakker et al., 2017).

Some other factors that may have an effect on bioerosion rates by sponges are light intensity, mechanical stimuli, current strength, diet supplementation and sediment load (Rützler, 1975; Duckworth & Peterson, 2013; Achlatis et al., 2017). Overall it is predicted that the impact of *C. celata* on oyster reefs will become even bigger in the future.

## Conclusion

By spatially visualizing the intracellular pH at the etching interface of *C. celata* we showed that acid production plays a role in clinoid sponge bioerosion. A reduction of the pH ( $\sim 6$ ) at this interface by the formation of low pH bundles is responsible for a change in the carbonate saturation state, which leads to dissolution of  $\text{CaCO}_3$  and over time to complex bioerosion patterns. From the obtained pH maps we were able to estimate a local proton flux of  $3.02 \times 10^{-8} \text{ mol dm}^{-2} \text{ s}^{-1}$  based on a form of the linear Heat-Diffusion equation that has been used before for foraminifera. As this is one of the first studies to visualize intracellular pH gradients in excavating sponges, no comparison with existing literature is possible yet. However, if we assume that all protons in this local flux will end up in the reaction with  $\text{CaCO}_3$ , we could estimate a local chemical bioerosion rate of  $\sim 0.11 \text{ mg cm}^{-2} \text{ h}^{-1}$ . This is higher compared to other clinoid sponges, likely due to different methodologies used to determine this rate. For further studies a fully 3D diffusion model might give more accurate results as the protons are very heterogeneously distributed in the tissue and the sponge surface is very irregular.

Most studies regarding excavating sponges examine the environmental control of bioerosion, while many uncertainties remain about the exact chemical conditions during sponge bioerosion. Here we showed that the use of HPTS as a fluorescent probe to visualize the pH with fluorescence microscopy is a successful method. This method could also be used for further studies with excavating sponges,

for example to investigate coral bioerosion, and makes it possible to compare bioerosion of different sponges at a molecular level. As bioerosion by *C. celata* occurs in successive phases, we would recommend to investigate the relation between the erosion development phase with the amount and locations of low pH bundles present. More data about sponge acidity over time would also result in a more reliable estimation of the proton flux. Altogether, when more data about chemical and physical conditions during sponge bioerosion becomes available, we are able to understand better why bioerosion is expected to increase with future climate scenarios and why excavating sponges become these successful macro-eroders in ecosystems with carbonaceous substrates.

## Acknowledgements

I would like to thank Paolo Stocci, Lennart de Nooijer and Gert-Jan Reichart for giving me the opportunity to work at NIOZ Texel and their help, time and constructive feedback to realize this research for my MSc thesis. This thesis taught me many new lab and modelling techniques, which I enjoyed very much. It also gave me the possibility to conduct my own fieldwork for the collection of *C. celata* infested oysters, which I really loved. I would like to thank Peter H. van Bragt, Ton Klerks and Marco Faasse again for collecting the oysters during SCUBA diving. Finally, I would like to thank the OCS department student room for their continuous support and encouragement during my thesis research.

## References

- Achlatis, M., Van Der Zande, R. M., Schönberg, C. H., Fang, J. K., Hoegh-Guldberg, O., & Dove, S. (2017). Sponge bioerosion on changing reefs: ocean warming poses physiological constraints to the success of a photosymbiotic excavating sponge. *Scientific Reports*, 7(1), 1-13.
- Bahr, L.M. & R. E. Hillman, R.E. (1967). Effects of repeated shell damage to gametogenesis in the American oyster, *Crassostrea virginica* (Gmelin). *Proc. Natl. Shellfish. Assoc.* 57:59–62.
- de Bakker, D. M., Webb, A. E., van den Bogaart, L. A., van Heuven, S. M., Meesters, E. H., & van Duyl, F. C. (2018). Quantification of chemical and mechanical bioerosion rates of six Caribbean excavating sponge species found on the coral reefs of Curaçao. *PloS one*, 13(5), e0197824.
- Barnes, B. B., Luckenbach, M. W., & Kingsley-Smith, P. R. (2010). Oyster reef community interactions: The effect of resident fauna on oyster (*Crassostrea* spp.) larval recruitment. *Journal of Experimental Marine Biology and Ecology*, 391(1-2), 169-177.
- Beck, M. W., Brumbaugh, R. D., Airoidi, L., Carranza, A., Coen, L. D., Crawford, C., ... & Guo, X. (2011). Oyster reefs at risk and recommendations for conservation, restoration, and management. *Bioscience*, 61(2), 107-116
- Bennema, F. P., Engelhard, G. H., & Lindeboom, H. (2020). *Ostrea edulis* beds in the central North Sea: delineation, ecology, and restoration. *ICES Journal of Marine Science*, 77(7-8), 2694-2705.
- Bennema, F. (2022). *Verspreidingsatlas Sponzen*. Stichting ANEMOON. <https://www.verspreidingsatlas.nl/S134121>
- Bjornerud, M. (2007). *De aarde*. Amsterdam; Pearson Education Benelux.
- Bower, S. M., McGladdery, S. E., & Price, I. M. (1994). Synopsis of infectious diseases and parasites of commercially exploited shellfish. *Annual Review of Fish Diseases*, 4, 1-199.
- Buschbaum, C., Buschbaum, G., Schrey, I., & Thieltges, D. W. (2007). Shell-boring polychaetes affect gastropod shell strength and crab predation. *Marine Ecology Progress Series*, 329, 123-130.
- Carballo, J. L., Sanchez-Moyano, J. E., & García-Gómez, J. C. (1994). Taxonomic and ecological remarks on boring sponges (Clionidae) from the Straits of Gibraltar (southern Spain): tentative bioindicators?. *Zoological Journal of the Linnean Society*, 112(4), 407-424.
- Carballo, J. L., Naranjo, S. A., & García-Gómez, J. C. (1996). Use of marine sponges as stress indicators in marine ecosystems at Algeciras Bay (southern Iberian Peninsula). *Marine Ecology Progress Series*, 135, 109-122.
- Carballo, J. L., & Bell, J. J. (2017). *Climate change, ocean acidification and sponges*. Cham: Springer International Publishing.
- Carl Zeiss. (2020). *Software Manual ZEISS ZEN 3.3 (blue edition)*. München: Author. [http://www.ladydavis.ca/uploads/ZEN3.3\\_blue%20edition-SoftwareManual.pdf](http://www.ladydavis.ca/uploads/ZEN3.3_blue%20edition-SoftwareManual.pdf)
- Cobb, W. R. (1969). Penetration of calcium carbonate substrates by the boring sponge, *Cliona*. *American Zoologist*, 9(3), 783-790.
- Cobb, W. R. (1975). Fine structural features of destruction of calcareous substrata by the burrowing sponge *Cliona celata*. *Transactions of the American Microscopical Society*, 197-202.
- Compton, R. G., Daly, P. J., & Houses, W. A. (1986). The dissolution of Iceland spar crystals: the effect of surface morphology. *Journal of colloid and interface science*, 113(1), 12-20.
- Davis, N. W., & Hillman, R. E. (1971). Effect of artificial shell damage on sex determination in oysters. *Proc Natl Shellfish Assoc.* 61:2.
- Duckworth, A. R., & Peterson, B. J. (2013). Effects of seawater temperature and pH on

- the boring rates of the sponge *Cliona celata* in scallop shells. *Marine Biology*, 160(1), 27-35.
- Dunn, R. P., Eggleston, D. B., & Lindquist, N. (2014). Oyster-sponge interactions and bioerosion of reef-building substrate materials: implications for oyster restoration. *Journal of Shellfish Research*, 33(3), 727-738.
- Fromont, J., Craig, R., Rawlinson, L., & Alder, J. (2005). Excavating sponges that are destructive to farmed pearl oysters in Western and Northern Australia. *Aquaculture Research*, 36(2), 150-162.
- Gast, G. J., Jonkers, P. J., Van Duyl, F. C., & Bak, R. P. M. (1999). Bacteria, flagellates and nutrients in island fringing coral reef waters: influence of the ocean, the reef and eutrophication. *Bulletin of Marine Science*, 65(2), 523-538.
- Govers, L. L., Lamers, L. P., Bouma, T. J., de Brouwer, J. H., & van Katwijk, M. M. (2014). Eutrophication threatens Caribbean seagrasses—An example from Curaçao and Bonaire. *Marine pollution bulletin*, 89(1-2), 481-486.
- Grant, R. E. (1826). *Notice of a New Zoophyte (Cliona Celata, Gr.) from the Frith of Forth*. Edinburgh New Phil J 1:78-81.
- Grégoire, C. (1961). Structure of the conchiolin cases of the prisms in *Mytilus edulis* Linne. *The Journal of Cell Biology*, 9(2), 395-400.
- Guida, V. G. (1977). The physiological ecology of the oyster-burrowing sponge symbiosis and the roles of symbioses in marine systems. PhD dissertation. North Carolina State University, Raleigh, NC.
- Holmes, K. E. (2000). Effects of eutrophication on bioeroding sponge communities with the description of new West Indian sponges, *Cliona* spp. (Porifera: Hadromerida: Clionidae). *Invertebrate Biology*, 119(2), 125-138.
- Hancock, A. (1849). On the excavating powers of certain sponges belonging to the genus *Cliona*; with descriptions of several new species, and an allied generic form. *Annals and Magazine of Natural History*, 3(17), 321-348.
- Hartman, W. D. (1957). Ecological niche differentiation in the boring sponges (Clionidae). *Evolution*, 294-297.
- Hartman, W. D. (1958). Natural history of the marine sponges of southern New England. *Bull Peabody Mus Nat Hist*. 12: 1-155.
- Hatch, W. I. (1980). The implication of carbonic anhydrase in the physiological mechanism of penetration of carbonate substrata by the marine burrowing sponge *Cliona celata* (Demospongiae). *The Biological Bulletin*, 159(1), 135-147.
- Hill, M., Walter, C., & Bartels, E. (2016). A mass bleaching event involving clionaid sponges. *Coral Reefs*, 35(1), 153-153.
- Jones, C. G., Lawton, J. H., & Shachak, M. (1994). Organisms as ecosystem engineers. In *Ecosystem management* (pp. 130-147). Springer, New York, NY.
- Kennedy, E. V., Perry, C. T., Halloran, P. R., Iglesias-Prieto, R., Schönberg, C. H., Wisshak, M., ... & Mumby, P. J. (2013). Avoiding coral reef functional collapse requires local and global action. *Current Biology*, 23(10), 912-918.
- Lee, H. Z., Davies, I. M., Baxter, J. M., Diele, K., & Sanderson, W. G. (2020). Missing the full story: First estimates of carbon deposition rates for the European flat oyster, *Ostrea edulis*. *Aquatic Conservation: Marine and Freshwater Ecosystems*, 30(11), 2076-2086.
- Lemasson, A. J., Fletcher, S., Hall-Spencer, J. M., & Knights, A. M. (2017). Linking the biological impacts of ocean acidification on oysters to changes in ecosystem services: a review. *Journal of Experimental Marine Biology and Ecology*, 492, 49-62
- Livingston, R. J., Howell, I. V., Robert, L., Niu, X., Lewis III, G. F., & Woodsum, G. C. (1999). Recovery of oyster reefs (*Crassostrea virginica*) in a Gulf estuary following disturbance by two hurricanes. *Bulletin of Marine Science*, 64(3), 465-483.

- Lynch, T. C., & Phlips, E. J. (2000). Filtration of the bloom-forming cyanobacteria *Synechococcus* by three sponge species from Florida Bay, USA. *Bulletin of Marine Science*, 67(3), 923-936.
- Neumann, A. C. (1966). Observations on coastal erosion in Bermuda and measurements of the boring rate of the sponge, *Cliona* LAMPA 1, 2. *Limnology and Oceanography*, 11(1), 92-108.
- Nicol, W. L., & Reisman, H. M. (1976). Ecology of the boring sponge (*Cliona celata*) at Gardiner's Island, New York. *Chesapeake Science*, 17(1), 1-7.
- de Nooijer, L. J., Toyofuku, T., Oguri, K., Nomaki, H., & Kitazato, H. (2008). Intracellular pH distribution in foraminifera determined by the fluorescent probe HPTS. *Limnology and Oceanography: Methods*, 6(11), 610-618.
- Paolisso, M., & Dery, N. (2010). A cultural model assessment of oyster restoration alternatives for the Chesapeake Bay. *Human Organization*, 69(2), 169-179.
- Perry, C. T., Murphy, G. N., Kench, P. S., Edinger, E. N., Smithers, S. G., Steneck, R. S., & Mumby, P. J. (2014). Changing dynamics of Caribbean reef carbonate budgets: emergence of reef bioeroders as critical controls on present and future reef growth potential. *Proceedings of the Royal Society B: Biological Sciences*, 281(1796), 20142018.
- Pomponi, S. A. (1979). Ultrastructure of cells associated with excavation of calcium carbonate substrates by boring sponges. *Journal of the Marine Biological Association of the United Kingdom*, 59(3), 777-790.
- Pomponi, S. A., & Meritt, D. W. (1990). Distribution and life history of the boring sponge *Cliona truitti* in the Upper Chesapeake Bay. *New perspectives in sponge biology*. Smithsonian Institution Press, Washington, DC, 313.
- Ramsby, B. D., Hoogenboom, M. O., Whalan, S., & Webster, N. S. (2018). Elevated seawater temperature disrupts the microbiome of an ecologically important bioeroding sponge. *Molecular Ecology*, 27(8), 2124-2137.
- Ramsby, B. D., Hoogenboom, M. O., Whalan, S., Smith, H. A., & Webster, N. S. (2018). The bioeroding sponge *Cliona orientalis* will not tolerate future projected ocean warming. *Scientific reports*, 8(1), 1-13.
- Rawlinson, L. (2000). Management of a bioeroding sponge on the pearl oyster, *pinctada maxima*. BSc honours thesis, Edith Cowan University, Perth, WA.
- Rosell, D., Uriz, M. J., & Martin, D. (1999). Infestation by excavating sponges on the oyster (*Ostrea edulis*) populations of the Blanes littoral zone (north-western Mediterranean Sea). *Journal of the Marine Biological Association of the United Kingdom*, 79(3), 409-413.
- van Rossum, G., & Drake, F. L. (2009). *Python 3 Reference Manual*. Scotts Valley, CA: CreateSpace.
- Rützler, K. (1971). Bredin-Archbold Smithsonian Biological Survey of Dominica: Burrowing sponges, Genus *Siphonodictyon* Bergquist, from the Caribbean. *Smithson. Contrib. Zool.* 77:1-37.
- Rützler, K., & Rieger, G. (1973). Sponge burrowing: fine structure of *Cliona lampa* penetrating calcareous substrata. *Marine Biology*, 21(2), 144-162.
- Rützler, K. (1975). The role of burrowing sponges in bioerosion. *Oecologia*, 19(3), 203-216.
- Van der Schaaf, V. A., & van Hateren, J. V. (1996). Modelling the power spectra of natural images: statistics and information. *Vision research*, 36(17), 2759-2770.
- Schindelin, J., Arganda-Carreras, I., Frise, E., Kaynig, V., Longair, M., Pietzsch, T., ... Cardona, A. (2012). Fiji: an open-source platform for biological-image analysis. *Nature Methods*, 9(7), 676-682.
- Schönberg, C. H., & Loh, W. K. (2005). Molecular identity of the unique symbiotic dinoflagellates found in the bioeroding

- demosponge *Cliona orientalis*. *Marine Ecology Progress Series*, 299, 157-166.
- Schönberg, C. H. (2008). A history of sponge erosion: from past myths and hypotheses to recent approaches. In *Current developments in bioerosion* (pp. 165-202). Springer, Berlin, Heidelberg.
- Schönberg, C. H. L., & Wisshak, M. (2012). The perks of being endolithic. *Aquatic Biology*, 17(1), 1-5.
- Scyphers, S. B., Picou, J. S., Brumbaugh, R. D., & Powers, S. P. (2014). Integrating societal perspectives and values for improved stewardship of a coastal ecosystem engineer. *Ecology and Society*, 19(3).
- Snowden, E. (2007). *Marine Life Information Network: Biology and Sensitivity Key Information Reviews*. Marine Biological Association of the United Kingdom. <https://www.marlin.ac.uk/species/detail/2188>
- Stefaniak, L. M., McAtee, J., & Shulman, M. J. (2005). The costs of being bored: effects of a clionid sponge on the gastropod *Littorina littorea* (L.). *Journal of Experimental Marine Biology and Ecology*, 327(1), 103-114.
- Sullivan, B. W., Faulkner, D. J., Matsumoto, G. K., He, C. H., & Clardy, J. (1986). Metabolites of the burrowing sponge *Siphonodictyon coralliphagum*. *The Journal of Organic Chemistry*, 51(24), 4568-4573.
- Thomas, P. A. (1979). Boring sponges destructive to economically important molluscan beds and coral reefs in Indian seas. *Indian Journal of Fisheries*, 26(1&2), 163-200.
- Topsent, E. (1887). Contribution à l'étude des clionides. *Arch. Zool. Exp. Gén.*, 5(2): 1-165.
- Toyofuku, T., Matsuo, M. Y., De Nooijer, L. J., Nagai, Y., Kawada, S., Fujita, K., ... & Kitazato, H. (2017). Proton pumping accompanies calcification in foraminifera. *Nature Communications*, 8(1), 1-6.
- Watabe, N. (1963). Decalcification of thin sections for electron microscope studies of crystal-matrix relationships in mollusc shells. *The Journal of Cell Biology*, 18(3), 701.
- Watabe, N. (1965). Studies on shell formation: XI. Crystal—matrix relationships in the inner layers of mollusk shells. *Journal of ultrastructure research*, 12(3), 351-370.
- Weisz, J. B., Massaro, A. J., Ramsby, B. D., & Hill, M. S. (2010). Zooxanthellar symbionts shape host sponge trophic status through translocation of carbon. *The Biological Bulletin*, 219(3), 189-197.
- Webb, A. E., van Heuven, S. M., de Bakker, D. M., van Duyl, F. C., Reichart, G. J., & de Nooijer, L. J. (2017). Combined effects of experimental acidification and eutrophication on reef sponge bioerosion rates. *Frontiers in Marine Science*, 4, 311.
- Webb, A. E. (2019). Reef dissolution: Rates and mechanisms of coral dissolution by bioeroding sponges and reef communities. PhD thesis. Utrecht University, Utrecht.
- Webb, A. E., Pomponi, S. A., van Duyl, F. C., Reichart, G. J., & de Nooijer, L. J. (2019). pH regulation and tissue coordination pathways promote calcium carbonate bioerosion by excavating sponges. *Scientific reports*, 9(1), 1-10.
- Weidgans, B. M. (2004). *New fluorescent optical pH sensors with minimal effects of ionic strength*. PhD thesis. University of Regensburg.
- Wisshak, M., Schönberg, C. H., Form, A., & Freiwald, A. (2012). Ocean acidification accelerates reef bioerosion. *PLoS One*, 7:e45124
- Wisshak, M., Schönberg, C. H., Form, A., & Freiwald, A. (2014). Sponge bioerosion accelerated by ocean acidification across species and latitudes?. *Helgoland Marine Research*, 68(2), 253-262.
- Zundelovich, A., Lazar, B., & Ilan, M. (2007). Chemical versus mechanical bioerosion of coral reefs by boring sponges—lessons from *Pione cf. vastifica*. *Journal of experimental biology*, 210(1), 91-96.

# Appendix

## Appendix A

Below follows a more elaborate step by step description for the creation of the pH maps, with the belonging python script code in grey text format:

In order to create pH maps from the grayscale images the modelling program Python (version Python3) was used. The following packages needed to be imported in the first code cell:

```
#Import packages

import PIL
from PIL import Image
import numpy as np
import matplotlib.pyplot as plt
```

Scanned images from the fluorescence microscope were imported in python and converted to a true grayscale, as the grayscale images from the ZEN environment were still in RGB format:

```
#Load scan images and convert to grayscale

ch1 = Image.open("blue.jpg").convert('L')
ch2 = Image.open("green.jpg").convert('L')
background = Image.open("white.jpg").convert('L')
```

In order to make calculations with the fluorescence scans, images were converted to an array where each location in the array represents a corresponding pixel intensity in the image:

```
#convert the true grayscale scan images to arrays

array_ch1 = np.asarray(ch1)
array_ch2 = np.asarray(ch2)
array_background = np.asarray(background)
```

To calculate the normalized ratio between the two fluorescence signals it is important to keep in mind that there can be 0 values (i.e. no fluorescence signal) present in the intensity arrays. This would result in errors when you divide the arrays with each other. To prevent this from happening a command was given to python to keep calculating the ratio for every location in the array. This eventually leads to a new ratio array containing NaN (Not a Number) values at locations where zero intensity was encountered in one of the intensity arrays. These NaN values were later replaced with a zero value:

```
#calculating the ratio in array format

np.seterr(divide='ignore', invalid='ignore')
ratio = array_ch1 / (array_ch1 + array_ch2)
ratio_nonan=ratio
ratio_nonan[np.isnan(ratio_nonan)] = 0
```

The ratio array was transformed to a pH array using Formula I obtained from the calibration curve. This was done stepwise by first calculating what was inside the natural logarithm. Negative and zero values inside this natural logarithm were replaced by 1, because otherwise it would be impossible to take the natural logarithm of these values. Then the pH was calculated by using the formula for all locations in the ratio array with positive values except value 1. For the locations in the ratio array where the factor inside the natural logarithm was set at 1 a pH value of zero would be returned in the for loop, which would later be replaced with a pixel from the light background:

```
#calculation the pH in array format

a=(0.38/(ratio_nonan-0.01)-1)
b=np.where(a>0,a,1)
height,width = ch1.size
print(height,width)
for j in range(height):
    for i in range(width):
        if b[i,j] != 1:
            pH_map[i,j] = 6.11-0.37*(np.log(b[i,j]))
        else: pH_map[i,j] = 0
pH=np.ma.masked_where(pH_map==0, pH_map)
```

The final step is to display the pH array on top of the background image so one can find spots with lower pH (Figure 19). For this a nearest neighbour interpolation was used:

```
#creating a pH map

fig = plt.figure()
plt.imshow(pH, alpha = 0.95, vmin=5, vmax=7.5, interpolation='nearest')
plt.imshow(array_background, cmap='gray', alpha=0.9)
plt.colorbar()
plt.show()
```

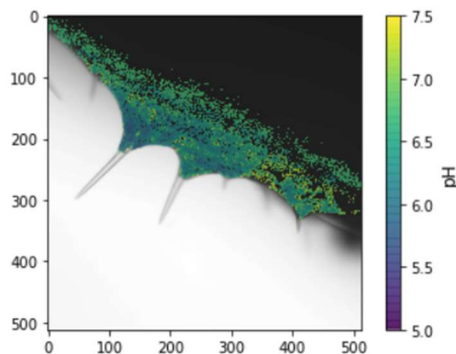


Figure 19: Example pH map output created in python.

This process was repeated for all scans created with the fluorescence microscope.

## Appendix B

Here follows an example to calculate the eroded volume of a SEM image with pits. From Figure 20 the depth of a pit is determined (22  $\mu\text{m}$ ). Not all pits have the same depth and dimensions but for this calculation it was assumed that all pits have a similar size. In ImageJ (Fiji) the surface area of all pits was determined (13022  $\mu\text{m}^2$ ), Figure 21. This led to an approximate eroded volume of  $3.65 \times 10^{-13} \text{ m}^3$ .

.....

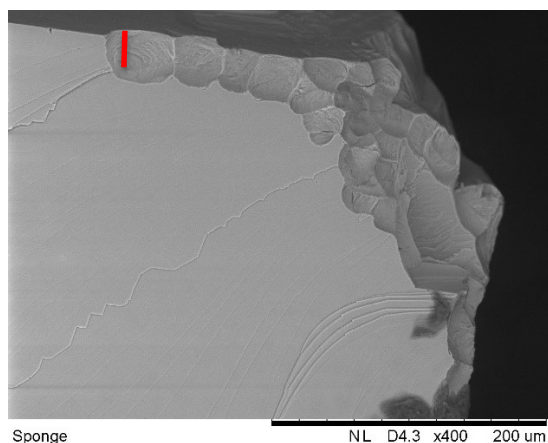


*Figure 20: Determination of pit depth (red line).*

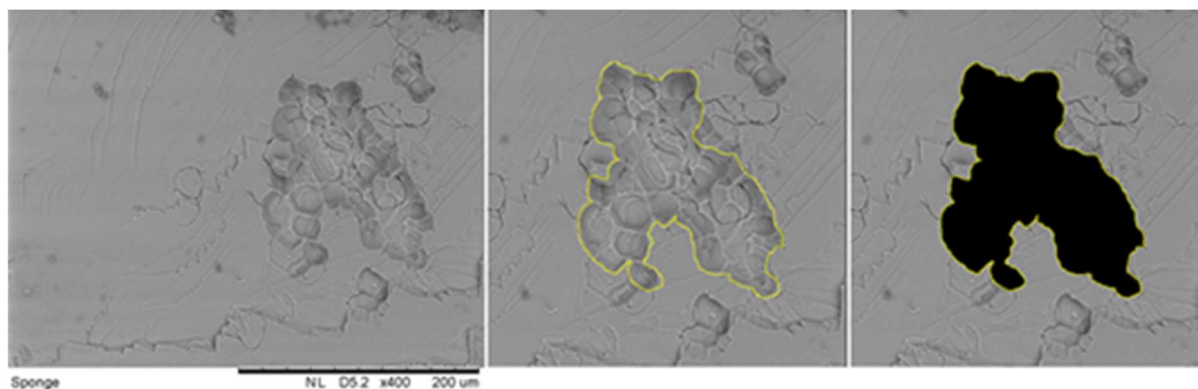


*Figure 21: Determination of eroded surface area.*

.....

Appendix C

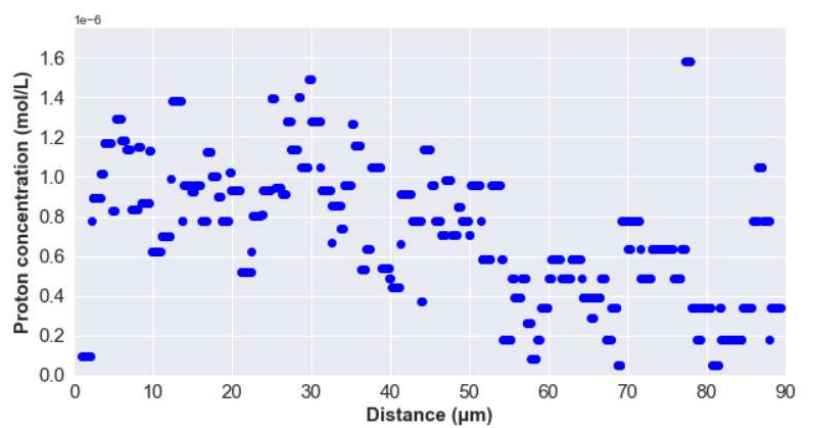
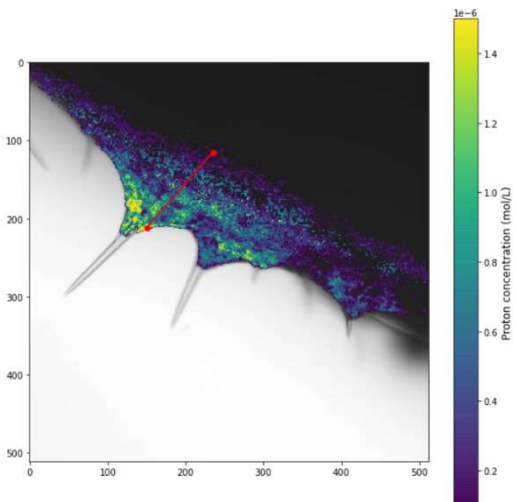
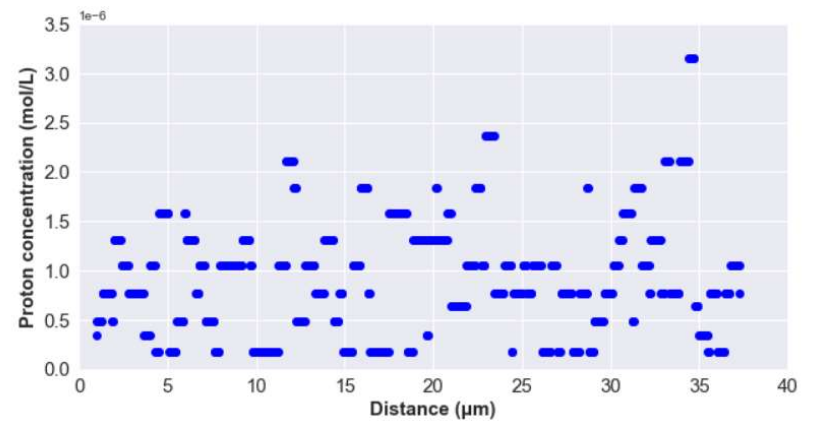
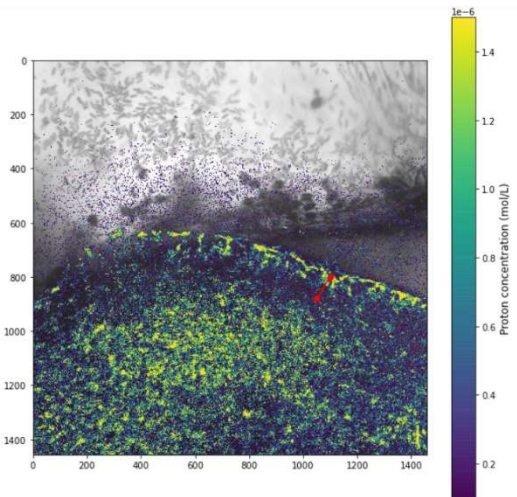
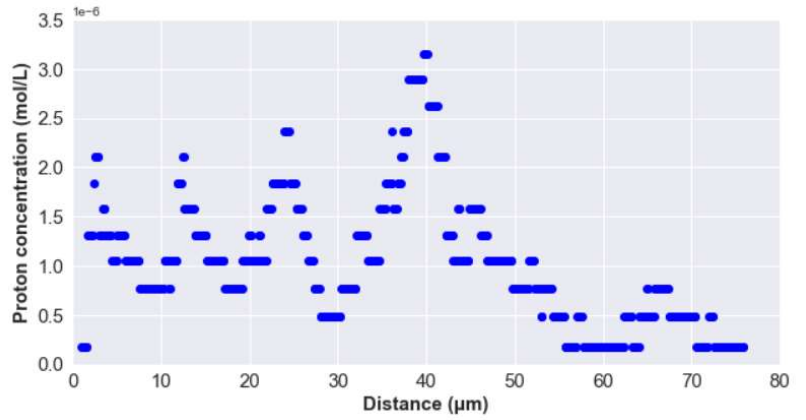
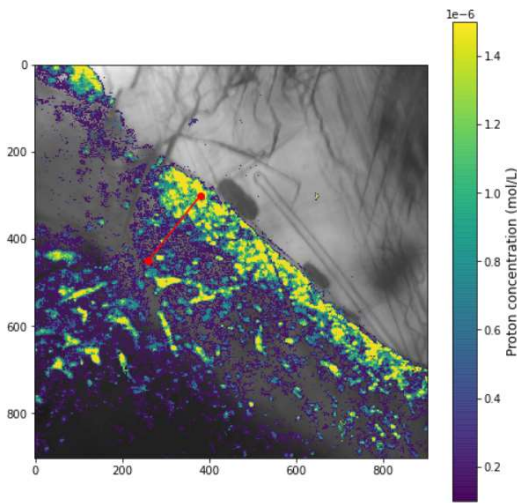


Figure 22: Proton concentration transects.